



**Universidad de los Andes**

PHYSICS DEPARTMENT

MEASUREMENT AND CHARACTERIZATION OF  
GRANULATION PATTERN IN THE IAG SOLAR FLUX  
SPECTRUM

**First version**

BSc Physics Final Project

**Author:**

Claudia Alejandra Cuellar Nieto

**Advisor:**

Benjamin Oostra Vannoppen

Nov 2025

## **Abstract**

Hello, this is my work:D

## **Acknowledgements**

# Contents

<b>List of Figures</b>	<b>3</b>
<b>1 Introduction: The Sun's granulation pattern</b>	<b>6</b>
1.1 Convective motion . . . . .	6
1.1.1 The three signatures of convection . . . . .	7
1.2 IAG Solar Flux Atlas . . . . .	8
1.3 IAG Spatially Resolved Quiet Sun Atlas . . . . .	8
1.4 Motivation . . . . .	9
<b>2 Literature Review: Convective motion in the Sun</b>	<b>10</b>
2.1 The solar interior and the solar outer atmosphere . . . . .	10
2.2 The solar convection Zone . . . . .	13
2.2.1 The convection movement in the sun . . . . .	13
2.2.2 Dynamics of solar convection . . . . .	13
2.2.3 The Schwarzschild criterion . . . . .	15
2.3 The Solar Photosphere . . . . .	16
2.3.1 Static photosphere: Limb darkening phenomenon . . . . .	16
2.3.2 Dynamic photosphere: The C-shaped profile bisector . . . . .	18
2.4 The three signature of convection . . . . .	19
2.4.1 First signature of convection: Line broadening . . . . .	19
2.4.2 Second signature of convection: Line profile bisector asymmetry . . . . .	20
2.4.3 Third signature of convection: Line depth-dependent wavelength shifts	21

2.4.4	Solar granulation pattern . . . . .	22
2.4.5	Chromodependence characterization . . . . .	23
<b>3</b>	<b>Methodology: The blend-free list of Fe I lines</b>	<b>27</b>
3.1	Computational approach . . . . .	27
3.2	Blend-free Fe I line Nave list . . . . .	28
3.2.1	Selection process for blend-free Fe I lines . . . . .	28
3.2.2	Observational requirement . . . . .	29
<b>4</b>	<b>Results and discussion: The three signatures of convection</b>	<b>30</b>
4.1	The first signature: Line broadening . . . . .	30
4.1.1	Line depth-dependence on line core curvature . . . . .	30
4.1.2	Line depth-dependence on lower excitation energy . . . . .	35
4.2	The second signature: Line profile bisector asymmetry . . . . .	40
4.2.1	The bisector slope . . . . .	40
4.2.2	Flux deficit (in progress) . . . . .	47
4.3	The third signature: Line depth-dependence on wavelength shifts . . . . .	49
4.3.1	The granulation pattern . . . . .	49
4.3.2	Characterization of chromodepence on granulation pattern . . . . .	54
4.4	Higher quality graphs . . . . .	58
<b>5</b>	<b>Conclusions</b>	<b>60</b>
<b>A</b>	<b>Z-score Standardization</b>	<b>61</b>
<b>B</b>	<b>The third derivate relation</b>	<b>63</b>
<b>C</b>	<b>Visualizer for outliers</b>	<b>65</b>
C.1	Test example . . . . .	65
C.2	Conditions justifications . . . . .	67

# List of Figures

2.1	The general structure of the Sun. Image modified from [1]. . . . .	11
2.2	The first clear photograph of the photosphere where the granulation pattern is visible. Image taken from [2] . . . . .	12
2.3	Diagram for the parcel of material displaced so slowly that remains in horizontal pressure. Image taken from [1] . . . . .	15
2.4	A view of granulation on the Sun's surface. The central regions exhibit blueshifts while the edges display redshifts. Image taken from [3] . . . . .	16
2.5	Squared profile for the disk intensity at increasing wavelengths. Image taken from [4] . . . . .	17
2.6	A time sequence showing granule evolution where the time intervals are about a minute. Image taken from [4] . . . . .	18
2.7	The C-curved line profile bisector. In the infrared shown to be less pronounced than violet range. . . . .	19
2.8	Asymmetries on an average absorption line. Can be observed the differences in intensity redshift profile. Image taken from [5] . . . . .	20
2.9	Granulation pattern for the IAG spatially resolved quiet sun atlas, is shown to have a strong chromodependence in the weaker lines. Image taken from [6]. .	22
2.10	Standard curve proposed by Gray and Oostra on the spectral range the spectral range of $4950\text{\AA}$ to $5700\text{\AA}$ . Image taken from [7]. . . . .	24
2.11	Contributions on angular momentum. Image taken from [4]. . . . .	25
4.1	Line core curvature for the Solar Flux Atlas separated in wavelength ranges. .	31

4.2	Line core curvature in the Solar Flux Atlas. The near infrared range presents a natural division due telluric lines in the atmosphere. . . . .	32
4.3	Linear polynomial fit applied to the range $(0.0 - 0.1)F/F_c$ of line depth in the visible range of the Solar Flux Atlas. . . . .	33
4.4	Line core curvature for the visible range for disk center data from the Spatially Resolved Quiet Sun Atlas. . . . .	34
4.5	First order polynomial fit applied to the range $(0.0 - 0.1)F/F_c$ of line depth in the visible range of the Spatially Resolved Quiet Sun Atlas. . . . .	35
4.6	Relative velocity against lower excitation energy for all the range in the Solar Flux Atlas . . . . .	36
4.7	Velocity bins of $100m/s$ around a fixed velocity, across the figure 4.6, with this separation is visible the energy shift across line depth. . . . .	37
4.8	Individual plots of lower excitation energy across line depth representing each bin of velocity for the Solar Flux Atlas. . . . .	38
4.9	Individual plots of lower excitation energy across line depth representing each bin of velocity for the Spatially Resolved Quiet Sun Atlas. . . . .	40
4.10	Line profile bisector slopes for the visible range in the Solar Flux Atlas. The behavior of the plot is according to the C-curved shape of the line bisector affected by convection movement. . . . .	42
4.11	First order polynomial fit adjusted to the range $(0.3 - 0.6)F/F_c$ for the line bisector slopes. . . . .	43
4.12	Line profile bisector slope for the visible range in the Spatially Resolved Quiet Sun Atlas. . . . .	44
4.13	First order polynomial fit adjusted to the range $(0.3 - 0.6)F/F_c$ for the line bisector slopes. . . . .	45
4.14	Line depth bins of 0.1 around a fixed depth, with this separation is visible the line bisector slope shift across wavelength. . . . .	46
4.15	Individual plots of line bisector slope shift across wavelength representing each bin of line depth for the Solar Flux Atlas. . . . .	46

4.16 Individual plots of line bisector slope shift across wavelength representing each bin of line depth for the Spatially Resolved Quiet Sun Atlas. . . . .	47
4.17 C-curved line profile bisector for the 6254.2850Å and the standard curve for the green range from the third signature plot. . . . .	48
4.18 Flux deficit curve for the 6254.2850Å and the temperatures of the mean, the maximum and the RMS point of the bisector. . . . .	49
4.19 Granulation pattern obtained for the Solar Flux Atlas. The wavelength shift dependence is along the line depth. . . . .	50
4.20 Comparision between atlases with velocity bins for the relation between wavelength and line depth. For each velocity bin was plotted wavelength against line depth to measure a frequency shift with a first order polynomial fit. . . .	51
4.21 Individual plots of lower excitation energy across line depth representing each bin of velocity. . . . .	52
4.22 Standard curve given by Gray and Oostra and recalculated for comparision with the current work. . . . .	54
4.23 Different color curves fitted to a specific range on granulation pattern for the visible range in the Solar Flux Atlas. The tendency on the curves is more pronounced in the violet and red range. . . . .	55
4.24 Different color curves fitted to a specific ranges on granulation pattern for the near infrared range in the Solar Flux Atlas. . . . .	57
4.25 We realized the same graphic for the comparision with the Ellwarth article to show the less scattered points. . . . .	58
4.26 Variance of the observed wavelength altering the number of points on the fourth order polynomial fit . . . . .	59

# Chapter 1

## Introduction: The Sun's granulation pattern

For decades, the solar spectrum has served as the fundamental reference point for spectroscopic analysis. As our nearest star, the Sun enables detailed studies of stellar composition. However, advances in optical instrumentation have revealed previously undetected spectral details, providing new insights into fundamental solar properties. One key insight is the granulation pattern caused by convective motion, which is characterized by three distinct hydrodynamic signatures: Line broadening, line bisector asymmetry, and the line-depth dependence of convective blueshift.

Inspired by David Gray's foundational research ([8] and references therein), this project aims to extract the granulation pattern from the IAG Solar Flux Atlas to calculate relative velocities and perform a detailed analysis based on the three signatures of convection.

### 1.1 Convective motion

The stellar spectrum serves as astronomy's primary source of information, encoding details about a star's composition and velocity. However, in some stars this spectrum is modified by fluid motions caused by density variations from temperature fluctuations in the outermost layer, where each spectral line exhibit a distinct velocity shift. These persistent convective

motions generate a granular structure in the solar photosphere, a phenomenon supported by extensive research (see [9, 10, 8]).

The granulation was first observed as a granular structure in movement by Janssen in 1855. Later, in 1901, Plaskett associated this pattern with the convective cells observed in Bénard's experiment [4], where fluids heated from below produces rising elements of hot gas convecting heat to the surface. This characteristic configuration gives the name *granulation* to all observable signs of solar convection.

### 1.1.1 The three signatures of convection

Convective motion produces three distinct signatures of granulation in stellar spectra: Line broadening, line bisector asymmetry, and line-depth dependence of convective blueshift [11]. This project focuses on the third signature, which exhibits a correlation between line depth and relative velocity. The method for quantifying this relationship is known as the *granulation pattern*, which means the plot of relative velocities against line depth [8].

The physical origin of this pattern lies in the convective process itself. When the Sun pushes material up through its outer layer, the spectrum exhibits a blueshift. As this material subsequently cools and falls back through the atmosphere, it produces a redshift but emits less light, making the blueshift dominant. Neutral iron lines (Fe I) are optimal for calibrating this phenomenon due to their high abundance, minimal thermal broadening, and limited isotopic variation. This approach offers the additional advantage of deriving natural wavelengths from a single source, thereby eliminating potential discrepancies.

The study of granulation patterns has been significantly documented by David Gray, whose work has improved the precision of stellar radial velocity measurements ([8] and references therein). This improvement stems primarily from his observation that granulation patterns in solar-type stars closely resemble the solar pattern, differing primarily by a scaling factor. This is particularly significant given the considerable challenges of obtaining such precise measurements for other stars, which are often affected by spectral noise, stellar proper motions, and velocity uncertainties [8]. Furthermore, analyzing solar granulation patterns is crucial for validating photospheric hydrodynamic models [10], enabling improved calibration and testing

of dynamic atmospheric models.

Following the motivation of treating the Sun as any other star, which does not have the proximity for spectra study, the most accurate solar flux atlas is necessary.

## 1.2 IAG Solar Flux Atlas

In 2016, Reiners and collaborators published the unprecedented precision *Institut für Astrophysik Göttingen (IAG)* Solar Flux Atlas obtained with the FTS *Fourier Transform Spectrograph* at Göttingen, simultaneously reporting convective blueshifts for a sample of Fe I lines. This atlas provides highly precise and accurate data, with radial velocity uncertainties on the order of  $\pm 10m/s$  across the wavelength range of 4050 to 10650 Å. In contrast to other FTS atlases, the entire visible wavelength range was observed simultaneously using only one spectrograph setting [12].

Despite the exceptional quality of the spectrum, the first derived granulation pattern appeared notably scattered and noisy. This was attributable to a rudimentary line position measurement methodology and a poorly line selection, which included numerous blended features, outdated wavelength references, and incomplete spectral coverage. Consequently, the full potential of the IAG atlas for determining precise convective blueshifts remains unrealized, highlighting the need for the refined analytical methods applied in this project.

## 1.3 IAG Spatially Resolved Quiet Sun Atlas

In 2023, Ellwarth and collaborators [6] published the *Institut für Astrophysik Göttingen (IAG)* Spatially Resolved Quiet Sun Atlas, also obtained with the FTS *Fourier Transform Spectrograph* at Göttingen. This atlas has the advantage of its coverage from the disc center ( $\mu = 1.0$ ) towards the solar limb ( $\mu = 0$ ), where  $\mu = \cos(\theta)$ . This spatial resolution enables the study of how convective blueshifts vary across the solar disc due to changing projection angles, a dependency that cannot be observed in other stars.

The principal objective of this project is to characterize the solar granulation pattern by treating

the Sun as any other star. To achieve this, the disk-integrated IAG Solar Flux Atlas serves as our primary data source. However, a precise analysis of the relative velocities in this integrated light requires correcting for the center-to-limb variations that are uniquely quantified by the Spatially Resolved Quiet Sun Atlas.

## 1.4 Motivation

In the first semester of 2025, Manuel Fuentes a physics student at the Universidad de los Andes, implemented these improvements in a computational project focused on the visible spectral range. By developing enhanced measurement techniques and employing a carefully curated line list that fully covers the visible range with updated wavelength references, Fuentes achieved significantly sharper granulation patterns than previous analyses. This work demonstrated that proper line selection and modern wavelength standards can reliably extract convective signatures from high-quality solar spectra.

Under the guidance of Professor Benjamin, this project extends the analysis into the near infrared range. This region contains spectral lines that originate from deeper photospheric layers. Although these lines are consequently weaker, they represent a rich source of information. However their analysis requires an adaptation of the existing measurement methodology. A key objective was to adapt these methods to enable the characterization of solar dynamics and line asymmetries via granulation patterns in the near infrared range.

By addressing these challenges, this project aims to produce a robust characterization of the solar granulation pattern and new insights into the photosphere's dynamic. These efforts are guided by the central research question: What are the direct spectroscopic consequences of solar dynamics?

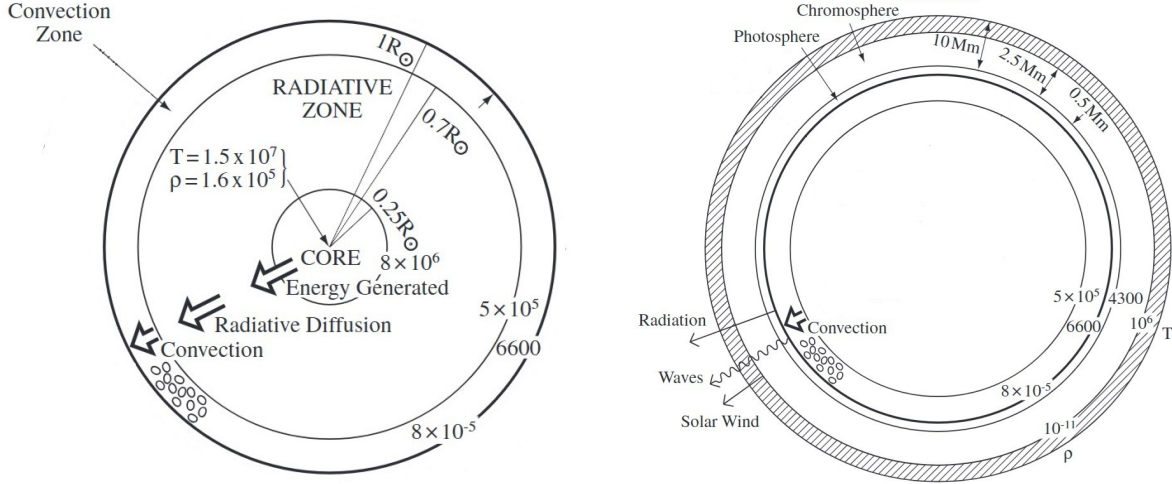
# **Chapter 2**

## **Literature Review: Convective motion in the Sun**

As previously mentioned, David Gray has significantly advanced the study of granulation patterns in the solar photosphere, with a particular focus on measuring relative velocities with high precision. This chapter explores the three signatures of convective motion in the Sun photosphere, and how this reveals the hydrodynamics on this outermost layer.

### **2.1 The solar interior and the solar outer atmosphere**

The Sun is classified as a yellow dwarf star of spectral type G2V. Its chemical structure is primarily composed of a large fraction of ionized hydrogen and a smaller proportion of helium. What makes the Sun unique in astronomical studies is its proximity to Earth, which allows for detailed observation unmatched for any other star. Structurally, the Sun is divided into two main regions: The solar interior and the solar outer atmosphere.



(a) The interior structure of the Sun. The convection zone is responsible for the general movement that characterizes the third signature.

(b) The outer structure of the Sun. The photosphere is the layer of the sun where the convection cells overshoot from the convection zone.

Figure 2.1: The general structure of the Sun. Image modified from [1].

As illustrated in the Figure 2.1a the overall structure of the solar interior is core, radiative and convective zone. Moving outward through these layers, both the density and temperature decrease significantly, as the energy is slowly transferred outwards by radiative diffusion. In the core, where energy is generated by thermonuclear fusion, standard models estimate a temperature of  $1.6 \times 10^7 K$  and density to  $1.6 \times 10^5 Kg/m^3$ . The extreme conditions in this region maintain the central material in a plasma state, functioning like a massive nuclear reactor.

This characteristic high density allows the absorptions and remissions of photons that make this zone highly opaque. This process, known as radiative diffusion, slowly transfers energy outward and progressively shifts the wavelength of the radiation from high-energy  $\gamma$ -rays to the visible light that eventually escapes.

On the other hand, the Figure 2.1b illustrates the overall structure of the solar outer atmosphere which consists of the photosphere, chromosphere and corona. In these layers, the density decreases rapidly with height above the solar surface. The temperature decreases to a minimum of approximately  $4300 K$  in the upper photosphere before rising through the chromosphere and transition region to millions of degrees in the corona. Thereafter, the temperature falls slowly

expanding outwards as the solar wind.

The most relevant layer for this project is the photosphere. This thin layer of plasma that emits most of the solar radiation and a continuous spectrum. When this continuous light passes through the overlying chromosphere, specific wavelengths are absorbed, resulting in the characteristic Fraunhofer lines superimposed on the continuum [1].

The target layers of this study are the convection zone and the photosphere, which will focus in further sections.

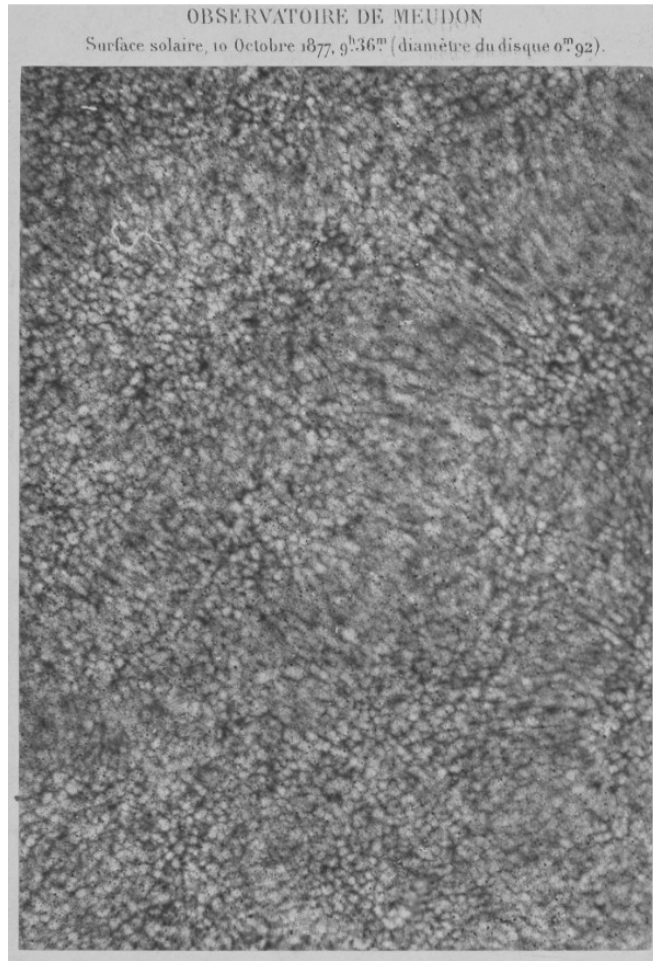


Figure 2.2: The first clear photograph of the photosphere where the granulation pattern is visible. Image taken from [2]

In 1885 Janssen obtained the first clear photograph of photospheric granules [2] providing the initial evidence for this granularar pattern (see figure 2.2) This was the starting point for dif-

ferent studies across the pattern of these granules. In 1930, Unsöld theorized that the layers beneath the photosphere should be convective unstable [4]. This hypothesis was later supported when Plaskett related the observed granules to the convective cells studied in Bénard's laboratory experiments [13]. In this analogy, a fluid heated from below develops rising elements of hot gas that transport heat to the surface.

These convective elements are known as granulation, with each individual region referred to as a granule. Typical granules span approximately 700 km and have short lifetimes, lasting between five to ten minutes. The understanding of granules as convective cells provided direct evidence for the existence of a zone responsible for convective motion beneath the photosphere.

## 2.2 The solar convection Zone

The convective zone, where dynamic plasma motions occur, begins at approximately  $0.86R_{\odot}$ . The great temperature gradient across this layer allows the convective process [1].

### 2.2.1 The convection movement in the sun

As previously mentioned, convection is driven by fluids heated from below representing hot rising gas elements or *convective cells* transporting heat to the photosphere [13]. In the solar context, convection takes place in a highly compressible and stratified gas. This physical regime leads to determine the conditions required for convection to occur and the resulting dynamics of the granules [4].

### 2.2.2 Dynamics of solar convection

From the core, He nuclei is built from H nuclei in the proton-proton chain as equation (2.1) refers.



The proton-proton chain reaction in the core liberates a considerable amount of energy in the

form of high-frequency  $\gamma$ -rays (approximately 26.7 MeV) and neutrinos (0.5 MeV). However, the strong Coulomb repulsion between positively charged nuclei, which increases with the product of their nuclear charges, means that only the lightest elements have appreciable fusion probabilities.

As energy is transported outward, photons are frequently absorbed and re-emitted. This process reduces the radiative conductivity, which in turn increases the temperature gradient [4]. When the transported energy reaches the low photosphere, a portion of the radiation escapes into space, and the plasma returns to a state of convective stability [1]. These conditions establish the onset of convection.

Consider a granule of plasma in local hydrostatic equilibrium with its surroundings, characterized by radial profiles of pressure  $P(r)$ , density  $\rho(r)$ , and temperature  $T(r)$ . If the granule's temperature is increased to a value  $T'$ , it will expand adiabatically to maintain pressure equilibrium, thereby decreasing its density relative to its surroundings.

This lower-density gas then experiences a buoyancy force, causing it to rise. The buoyancy force persists until the granule's density matches that of its new surroundings after traveling a mixing length  $l$ . Let  $T'_n$  be the temperature of the rising element and  $T_n$  the temperature of its new surroundings. The difference between the adiabatic gradient of the element and the radiative gradient of the surroundings governs the convection, as described by the equation (2.2)

$$T_n = T + \left( \frac{dT}{dr} \right)_R l \quad | \quad T'_n = T' + \left( \frac{dT}{dr} \right)_{ad} l \quad (2.2)$$

Where  $R$  refers for radiative temperature gradient and  $ad$  for the adiabatic temperature gradient. Convection occurs when the radiative gradient becomes steeper than the adiabatic gradient. Since we have assumed radiative equilibrium, the  $R$  denotes the gradient present in the stellar atmosphere.

The onset of convection leads to the inequality (2.3), where two conditions can arise: The convection pattern is established when radiative gradient exceeds the adiabatic gradient; otherwise, the layer is stable and energy is transported by radiation.

$$-\left( \frac{dT}{dr} \right)_R > \left( \frac{dT}{dr} \right)_{ad} \quad (2.3)$$

If the convective pattern is established, the element continues to expand adiabatically as it rises, driven by buoyancy. Otherwise, if the layer is stable, the element will contract, becomes heavier than its surroundings and begins to move down toward its original position.

This onset of instability, when the vertical temperature gradient is too large, is formally described by the Schwarzschild criterion for convection.

### 2.2.3 The Schwarzschild criterion

Taking the element described before, now suppose an elementary parcel of material displaced so slowly that remains in horizontal pressure equilibrium (see figure 2.3).

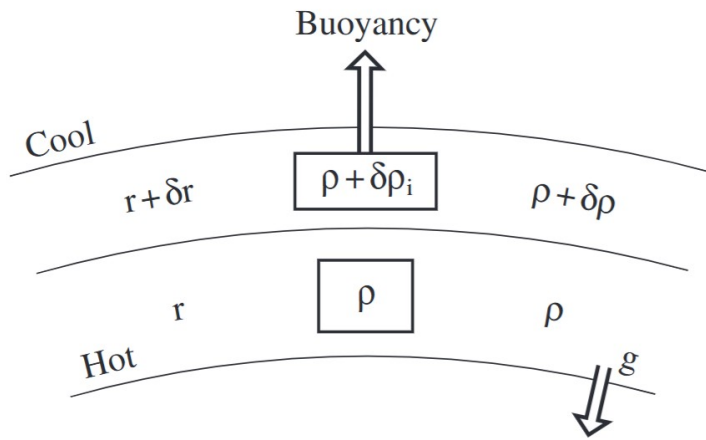


Figure 2.3: Diagram for the parcel of material displaced so slowly that remains in horizontal pressure. Image taken from [1]

If the motion is adiabatic there is no heat exchange with surroundings, the pressure and density of the rising element are adiabatic. This generates a criterion for the presence of convection known as the Schwarzschild criterion (2.4).

$$-\frac{dT}{dr} > \frac{\gamma - 1}{\gamma} \left( \frac{GM_{\odot}m}{r^2 k_B} \right) \quad (2.4)$$

Where  $k_B$  refers to Boltzmann constant;  $G$  the gravitational constant;  $M_{\odot}$  the solar mass;  $m$  the mass of the granule; and  $\gamma$  the adiabatic index. The presence of convection reduces the temperature gradient from the higher value required for purely radiative transport to a adiabatic

value [4]. The material and energy transported by this process ended up to low photosphere, where the granules exhibit different properties that will be examined in subsequent sections.

## 2.3 The Solar Photosphere

Since 1874, when Langley gave a detailed description of granulation on the photosphere, astronomers have studied the dynamics and reactions within Sun's outermost layer [1]. A distinct pattern of granules with dynamic behavior is apparent, where individual cells continuously emerge and disappear (see Figure 2.4).

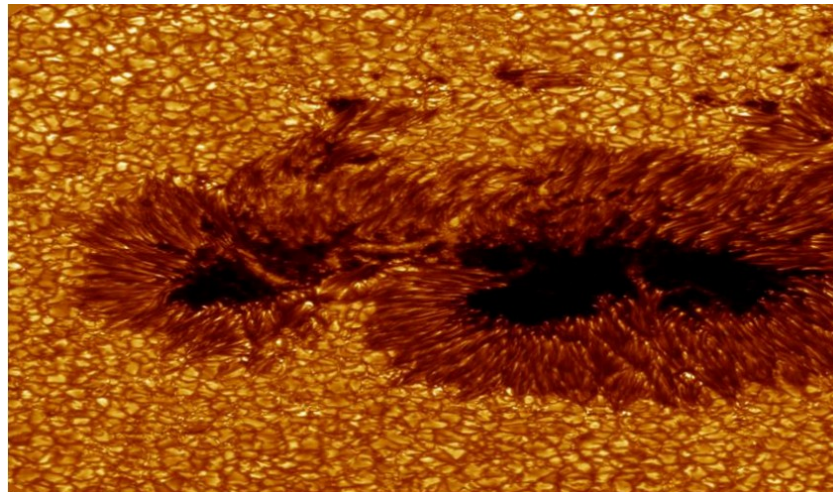


Figure 2.4: A view of granulation on the Sun's surface. The central regions exhibit blueshifts while the edges display redshifts. Image taken from [3]

The bright areas of granules correspond to regions where hot gas rises through the solar atmosphere. As this gas releases energy in the form of photons at the photosphere, it cools and subsequently descends, creating the darker regions of granules [14].

### 2.3.1 Static photosphere: Limb darkening phenomenon

Because the temperature decreases outward through the photospheric layers, the observed intensity falls off towards the solar limb. This effect is known as *Limb darkening phenomenon*,

discovered by Halm in 1907 [10] also causes the disk intensity profile to appear more squared at increasing wavelength (see Figure 2.5).

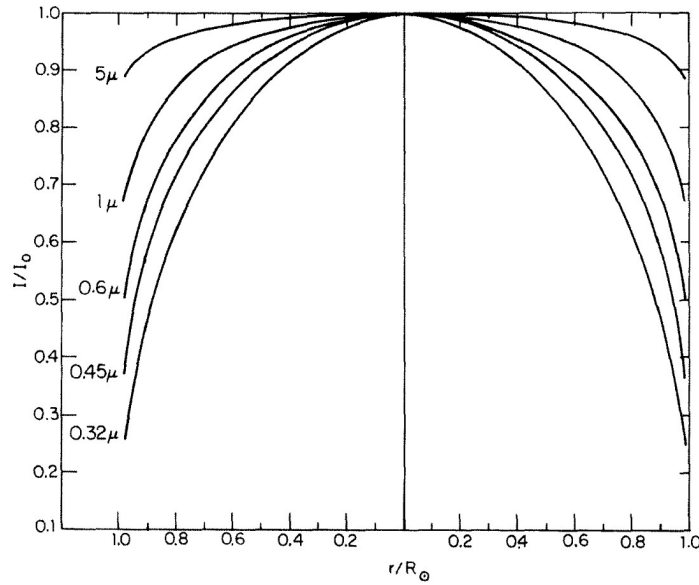


Figure 2.5: Squared profile for the disk intensity at increasing wavelengths. Image taken from [4]

The analysis of this effect provides a direct technique for determining the temperature structure of the photosphere as a function of depth.

Furthermore, high-resolution observations reveal that these granules have shown to be in continual motion (see Figure 2.6).

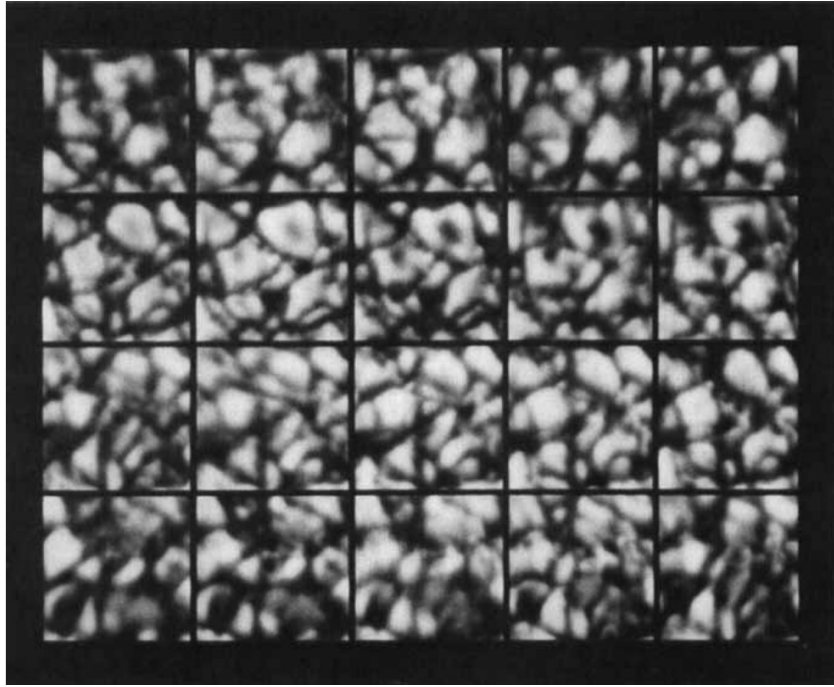


Figure 2.6: A time sequence showing granule evolution where the time intervals are about a minute. Image taken from [4]

This perpetual motion across the photosphere generates asymmetries in absorption line profiles. For typical weaker lines, the convective blueshift diminishes toward the limb, with a net velocity change approximately of  $400\text{m/s}$ . As explained by Ellsworth et al., observations closer to the limb pass through the atmosphere at a shallower angle. This results in longer optical paths through high atmospheric layers, allowing the gravitational redshift to dominate the measured signal [6].

### 2.3.2 Dynamic photosphere: The C-curved profile bisector.

Analysis of granule dynamics reveals a height dependence of convective velocities: The vertical velocity of a rising granule decays less rapidly than its excess brightness. Changes in the granulation structure, contrast and velocity field around the spots and magnetic network have been inferred indirectly from observations of Fraunhofer line profile shapes [4]. A direct result of the correlation between brightness and velocity of granules is the characteristic C-shaped line profile bisector observed in photospheric absorption lines (see figure 2.7).

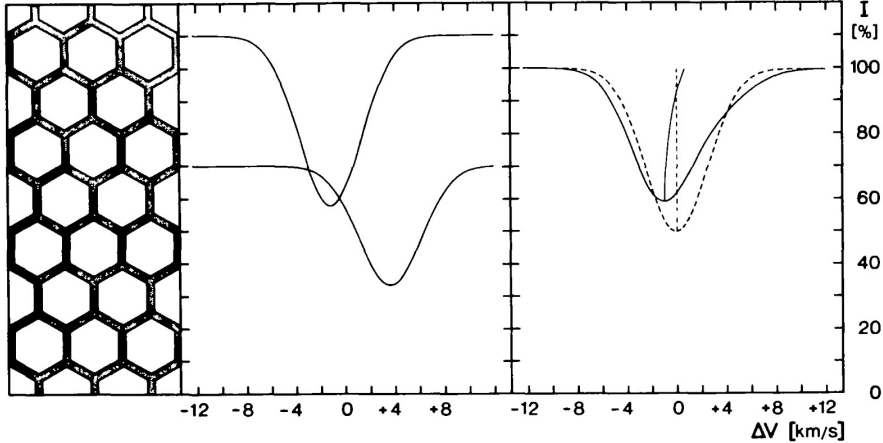


Figure 2.7: The C-curved line profile bisector. In the infrared shown to be less pronounced than violet range.

The formation of the C-curved line profile bisector occurs in three stages, corresponding to different heights in the photosphere.

First, the mid-depth portion of the line profile is formed in the brightest upflowing material, resulting in a blueshift. Then, the deepest part of the line core is formed higher up, in a region of decelerated upflow, producing a smaller blueshift. Finally, the line wings where the opacity is lowest, tend to be formed deepest in the cool material, resulting in a redshift.

This dynamic process induces characteristic perturbations in spectral lines, manifesting as line broadenings, line profile asymmetries, and line depth-dependent wavelength shifts known as the three signatures of convection [11].

## 2.4 The three signature of convection

The signatures of convection in stars are described by Gray in his research [8, 7, 11] as the principal characteristics to identify and treat the asymmetries due to convective motion.

### 2.4.1 First signature of convection: Line broadening

Due to the limb darkening phenomenon and atmospheric absorption, there exists two types of line cores: Strongest and weaker lines [11]. In general, stronger absorption lines exhibit more

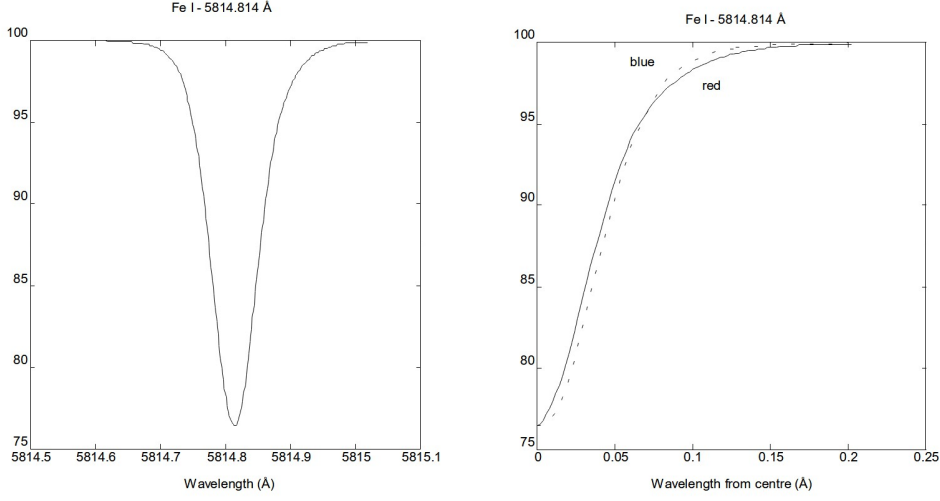


Figure 2.8: Asymmetries on an average absorption line. Can be observed the differences in intensity redshift profile. Image taken from [5]

pronounced core curvature than weaker lines. This line core curvature  $C_c$  can be quantified by the second derivative of the line's intensity profile with respect to wavelength, evaluated at observed wavelength (see equation (2.5)).

$$C_c = \lambda_{obs}^2 \left( \frac{d^2 p(\lambda_{obs})}{d \lambda_{obs}^2} \right) \quad (2.5)$$

In the near infrared range, the solar spectrum contains natural bands or groups of lines that are separated by regions of strong absorption from telluric elements. In other words, elements like  $O_2$  and  $CO_2$  that are absorbed by the atmosphere. This phenomenon can alter the line core curvature of determining lines profiles, specially in the near infrared range.

#### 2.4.2 Second signature of convection: Line profile bisector asymmetry

As demonstrated by Nieminen [5], the asymmetry occurs because the c-curved profile bisector reflects velocity variations and a bisector slope (see figure 2.8).

According to Kirchhoff's laws, absorption line formation requires lower temperature conditions, which are found precisely in the Sun's outermost atmospheric layers [14]. These regions not only provide the appropriate temperatures for absorption but also exhibit comparatively

higher opacity. Among all available spectral lines, those from Fe I are particularly valuable for solar granulation studies due to two key characteristics: They display significant opacity and relatively low thermal broadening. These properties make Fe I lines excellent tracers of granulation patterns in the solar photosphere [5].

These asymmetries imprinted on these Fe I lines can be quantified by analyzing their bisectors. A powerful method for this involves using the third derivative of the line profile, which provides a measure of the bisector's shape and curvature (see Equation (2.6)). The relation presented is described in appendixB.

$$\frac{c}{\lambda_{obs}} \left( \frac{1}{3C_c^2} \right) \left( \frac{d^3 p(\lambda_{obs})}{d\lambda_{obs}^3} \right) \quad (2.6)$$

Since most of stellar observations are made with lower-resolution spectrographs and often lower signal-to-noise ratios, there is a need to study granulation through its signatures. Gray and Oostra identified a form of line profile asymmetry observable under these conditions, known as the *flux deficit*. This phenomenon can be interpreted as flux imbalances on the red-shifted side of the line profile, caused by a net loss of radiative energy. Consequently, the line's bisector becomes inclined relative to its original, symmetric position.

To quantify this asymmetry, the authors proposed calculating the flux deficit by taking the difference between the observed, altered profile and a reference symmetric profile. By treating the altered line profile as an approximate representation of the third signature of convection, one can observe the flux difference interpreted as radiation [7].

### 2.4.3 Third signature of convection: Line depth-dependent wavelength shifts

Many studies across the years have detected and observed the phenomena of wavelength shifts against the line depth, or as it is called, chromodependence in the granulation pattern. This behavior was shown to be more present in the weaker lines which are related to infrared and violet range.

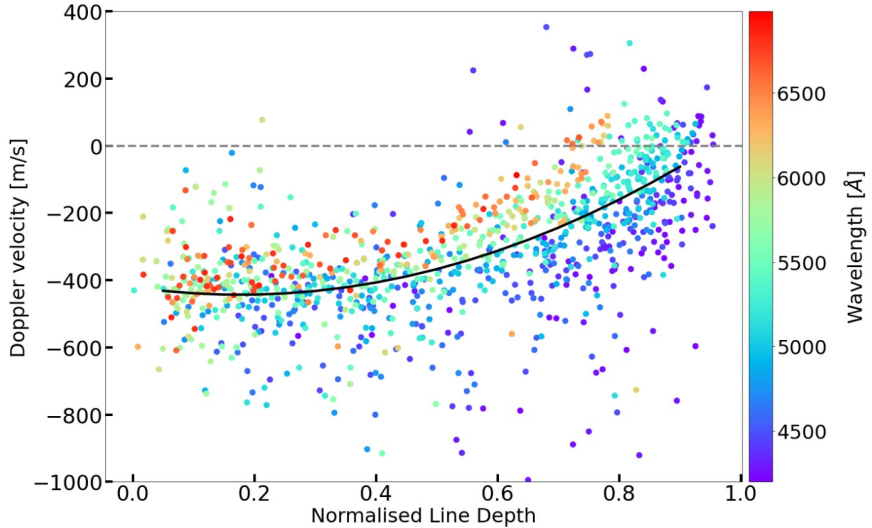


Figure 2.9: Granulation pattern for the IAG spatially resolved quiet sun atlas, is shown to have a strong chromodependence in the weaker lines. Image taken from [6].

#### 2.4.4 Solar granulation pattern

The solar granulation pattern is a plot of relative velocity against line depth, as shown in the Figure 2.9.

The significance of the granulation pattern lies in its universality for solar-type stars; their patterns closely resemble the Sun's, differing primarily by a scaling factor (see [11]). Consequently, a detailed analysis contributes to the understanding and radiation of photospheric hydrodynamic models [10, 8]. However, a precise measurement of the granulation pattern requires a understanding of the convective blueshift phenomenon.

#### Convective Blueshift

When the Sun pushes material up through its outer layer, the spectrum exhibits a blueshift. As this material subsequently cools and falls back through the atmosphere, it produces a redshift, but emits less light, making the blueshift dominant. That can be measure by the Doppler effect but as the velocities can be significant, the relativistic formulation of this effect must be applied.

The relativistic Doppler effect accounts for length contraction, as predicted by Einstein's theory

of relativity. This introduces an additional correction term to the classical shift, which becomes particularly relevant in high-velocity scenarios or strong gravitational fields. However, the measured negative redshift resulting from convective motions is known as *convective blueshifts* which are measured by the equation (2.7).

$$v_r \approx c \left( \frac{\lambda_{obs} - \lambda_{rep}}{\lambda_{rep}} \right) \quad (2.7)$$

Since the strength of the convective distortions and shifts as spectral lines vary across the H-R diagram, we expect systematic errors in radial velocities [8].

#### 2.4.5 Chromodependence characterization

Recent emphasis on measuring the granulation pattern has led to new interpretations of line depth-dependent wavelength shifts. However, a comprehensive characterization of this phenomenon is still missing.

In 2018, Gray and Oostra attempted to establish a standard curve determined by a third order polynomial fit to the solar granulation pattern (see figure 2.10).

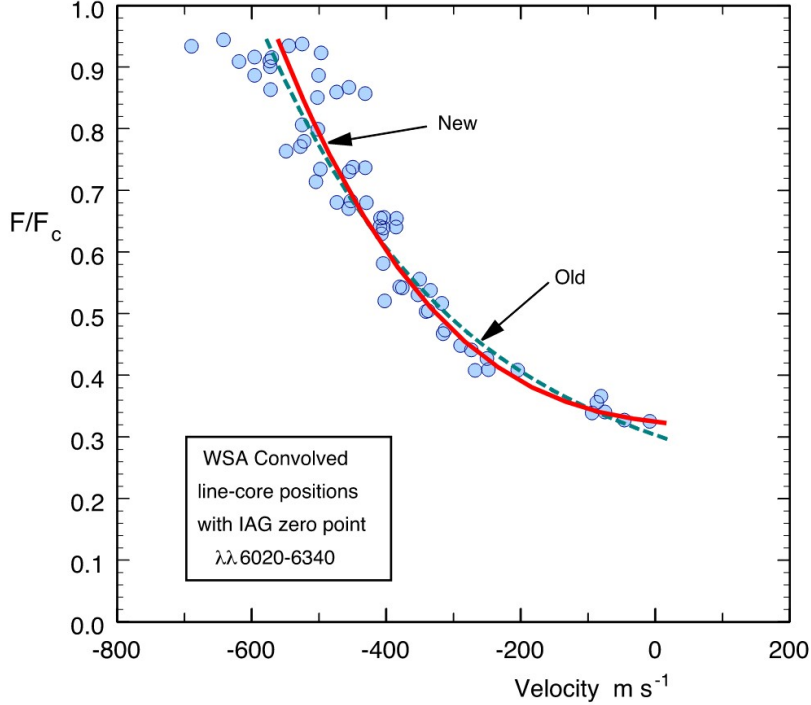


Figure 2.10: Standard curve proposed by Gray and Oostra on the spectral range the spectral range of  $4950\text{\AA}$  to  $5700\text{\AA}$ . Image taken from [7].

Nevertheless, the authors limited the spectral range of  $4950\text{\AA}$  to  $5700\text{\AA}$ , thereby avoiding the chromodependence in weaker lines. This limitation motivates the present work to develop a strong characterization and give the methodology for dealing with this phenomenon.

A separate theoretical perspective, offered by Hamilton and Lester, attributes aspects of photospheric dynamics to rotation. The pronounced differential rotation with latitude observed seems to be the result of convective flows driven radially by the buoyancy force and deflected horizontally by the Coriolis force [4]. This rotation contributes to angular momentum through two forms: Meridional circulation and Reynolds stresses.

The first contribution involves axisymmetric meridional circulation (see Figure 2.11). In the absence of other transport mechanism, such a circulation would tend to spin up the poles and the interior, as the moving fluid conserves its angular momentum.

The second contribution, which tends to enforce solid body rotation, arises from Reynolds stresses associated with nonaxisymmetric convective motions. The mechanism can be un-

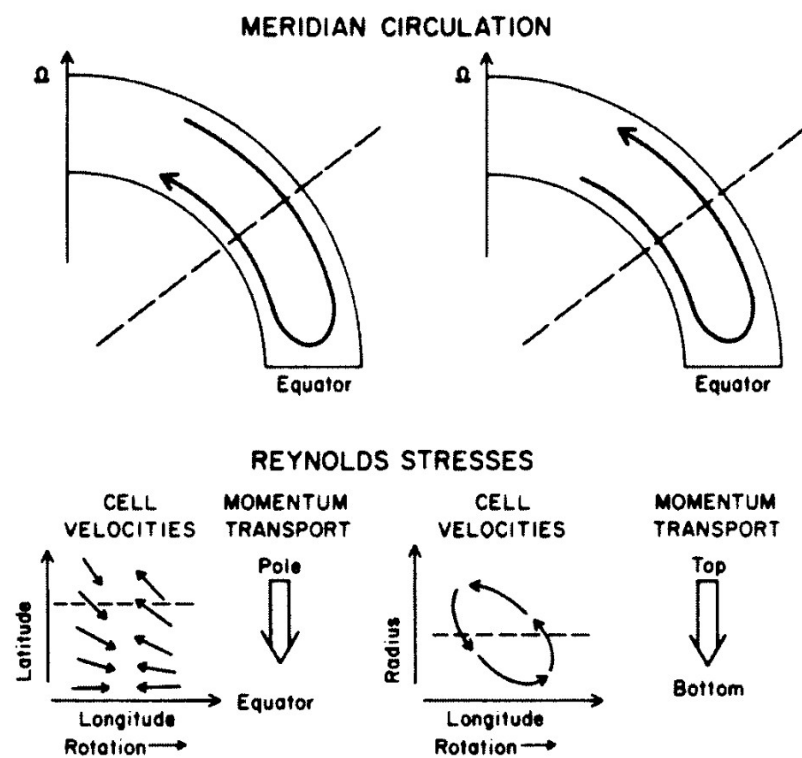


Figure 2.11: Contributions on angular momentum. Image taken from [4].

derstood by considering that, for equal velocities in the meridional plane, the flux of angular momentum per unit mass is greater toward the equator than away from it. This process depends critically on nonaxisymmetric convection, as it generates net fluxes of angular momentum in latitudinal and radial directions without a corresponding net mass flux. Neither buoyancy forces, which are strictly radial, nor pressure gradients, which must average to zero around the solar circumference, can directly influence the sun's axisymmetric rotation profile [4]. Therefore, the combined action of meridional circulation and Reynolds stresses is essential for shaping the observed differential rotation.

# Chapter 3

## Methodology: The blend-free list of Fe I lines

Given the complexity introduced by convective motions on the spectrum, this project takes a computational approach leading to an observational requirement, guided by Professor Benjamin's experience and previous research. The analysis was conducted using the Python programming language. All data and code have been uploaded in a [GitHub repository](#), allowing anyone interested to reproduce the results and verify the authenticity of the conclusions presented.

This project follows the methodology established in previous studies (see [10] and references therein), utilizing a selected list of Fe I lines from Nave [15]. As previously discussed, these lines are ideal for the calibration process due to their minimal thermal broadening and reduced susceptibility to other atmospheric perturbations.

### 3.1 Computational approach

The computational approach focuses on identifying the solar granulation pattern by calculating relative velocities from Fe I lines.

The line up was to identify the Fe I lines in the IAG Solar Flux Atlas and the IAG Spatially Resolved Quiet Sun Atlas using the blend-free list from Nave list of Fe I lines [15]. For each

identified line were selected bins of  $0.1 m\text{\AA}$  around the closest minimal point to the associated value from the Nave Fe I list. Beware, these points are not the observed wavelengths, just a reference to generate an observation window. Then, a fourth-order polynomial fit was adjusted due to the wavelength window and found the minimal point, whose represent the observed wavelength. The efficacy of this approach for quantifying asymmetry via the bisector slope is supported by [16]. For an optimal fit was used a z-score standardization on each line core, which is explained in appendix A. The observed wavelength from the polynomial fit was used to calculate the relative velocity. Finally, the values for the line core curvature (see equation (2.5)) and the line core bisector slope (see equation (2.6)) were found.

## 3.2 Blend-free Fe I line Nave list

The mention line up implemented the Nave list of laboratory-measured Fe I lines [15]. This list classifies lines with a quality rating (A,B,C,D), where A denotes the highest quality and reliability. However, not all the cataloged lines are clearly present in the solar spectrum, and within the near-infrared range, many lines are severely blended.

In collaboration with Professor Benjamin and Manuel Fuentes, we refined this initial list using different approaches to select the most reliable values.

### 3.2.1 Selection process for blend-free Fe I lines

The line selection process employed two approaches: Computational and visual. Initially, only quality A lines for the Nave list were selected. This group were subjected to four computational filters based on the properties of having a fourth-order polynomial fit for the line core.

The first filter takes into account the form of the C-curved line profile bisector. Lines whose bisectors exhibited excessive scatter, indicating a profile dominated by noise rather than a convective signature, were rejected.

The second filter selected lines whose curvature sign was consistent with an absorption line; this implies the coefficient of the fourth-order term needs to be positive. A filter based on the magnitude of these coefficients was intentionally avoided. This is because weaker lines, which

are essential for a complete analysis, have smaller curvature, and lines in the near infrared range exhibit large curvatures related to blending with telluric atmospheric lines.

The third filter ensure the selected lines represented an absorption curve by discarding closest points that more closely resemble slopes or continuum noise. The condition was filter lines which the difference between extreme points of the fit was less than half of the line depth.

The final filter required the absolute difference between the observed wavelength and the measured laboratory wavelength to be less than  $0.025\text{\AA}$ . Larger discrepancies suggest misidentification or severe blending, rendering the calculated relative velocity unreliable. This threshold is empirically supported by observations throughout the selection process and the statement for the mean velocity of the sun is  $200 - 600m/s$ .

### 3.2.2 Observational requirement

The final part of the selection process was a visual inspection to discard lines that were blended or absent from the solar spectrum. A custom visualizer (detailed in appendixC) was instrumental for this, allowing the simultaneously display of graphics related to dynamics aspects. This was particularly useful for selection lines in the near-infrared range. The visual requirement focused on the geometry of the spectral line profile, its behavior on the three signatures plots and the guidance from professor Benjamin.

The concluding part of the methodology was performed the plots which represents the three signatures of convection.

First of all, the granulation pattern (relative velocity), core curvature and core bisector against line depth was performed to all ranges in both atlases with the objective to observe the three signatures of convection. Subsequently, various parameters were plotted against line depth to specifically characterize the phenomenon of chromodependence.

# **Chapter 4**

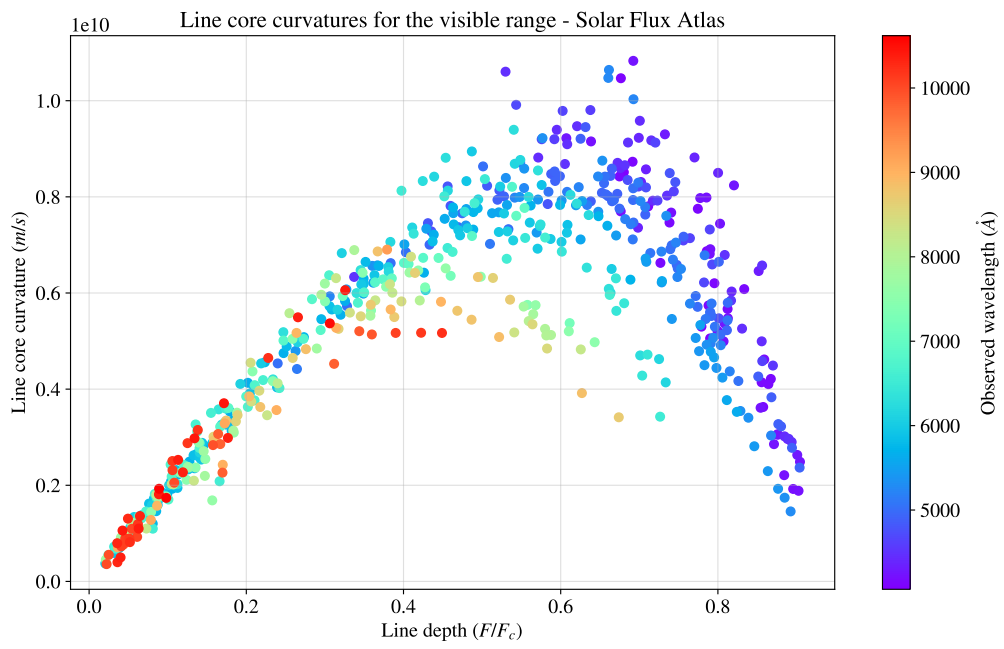
## **Results and discussion: The three signatures of convection**

Our results were separated into the three signatures of convection around the main phenomenon of chromodependence.

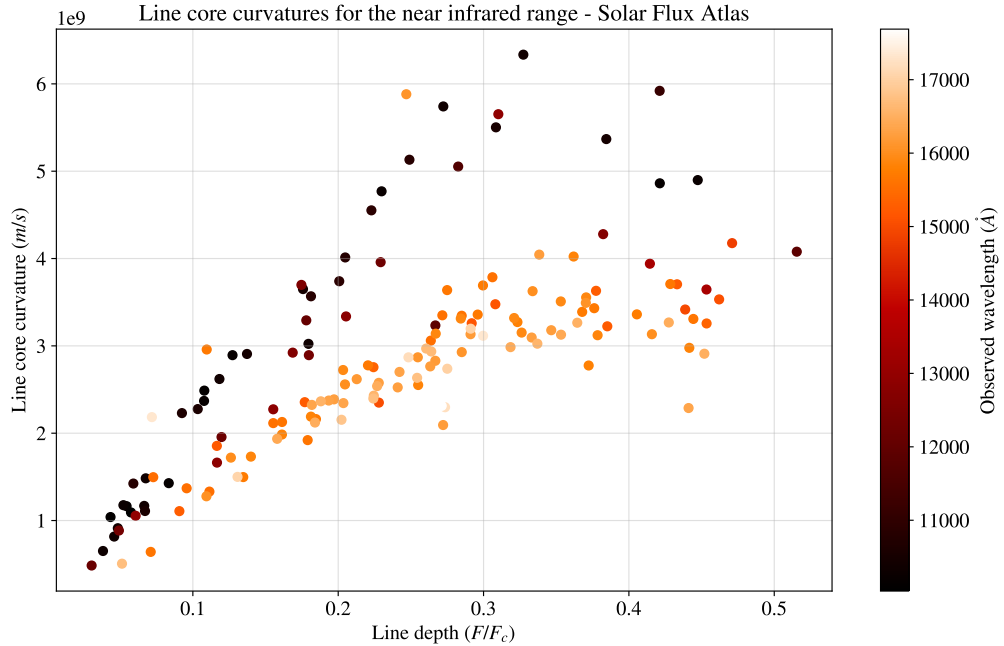
### **4.1 The first signature: Line broadening**

#### **4.1.1 Line depth-dependence on line core curvature**

The core curvature was calculated following the equation (2.5) and plotted against line depth as shown in figure 4.1.



(a) Line core curvature for the visible range in the Solar Flux Atlas. Is visible a characteristic curve with line depth-dependence along wavelength.



(b) Line core curvature for the near infrared range in the Solar Flux Atlas. Is visible a natural division for wavelengths in 11400 $\text{\AA}$ .

Figure 4.1: Line core curvature for the Solar Flux Atlas separated in wavelength ranges.

As shown in Figure 4.1b, the near infrared range exhibits a natural division at approximately  $11400\text{\AA}$ , a region dominated by telluric absorption lines from Earth's atmosphere. When plotting the entire spectral range of the Solar Flux Atlas, a clear line depth-dependence of the convective blueshift as a function of wavelength is observed.

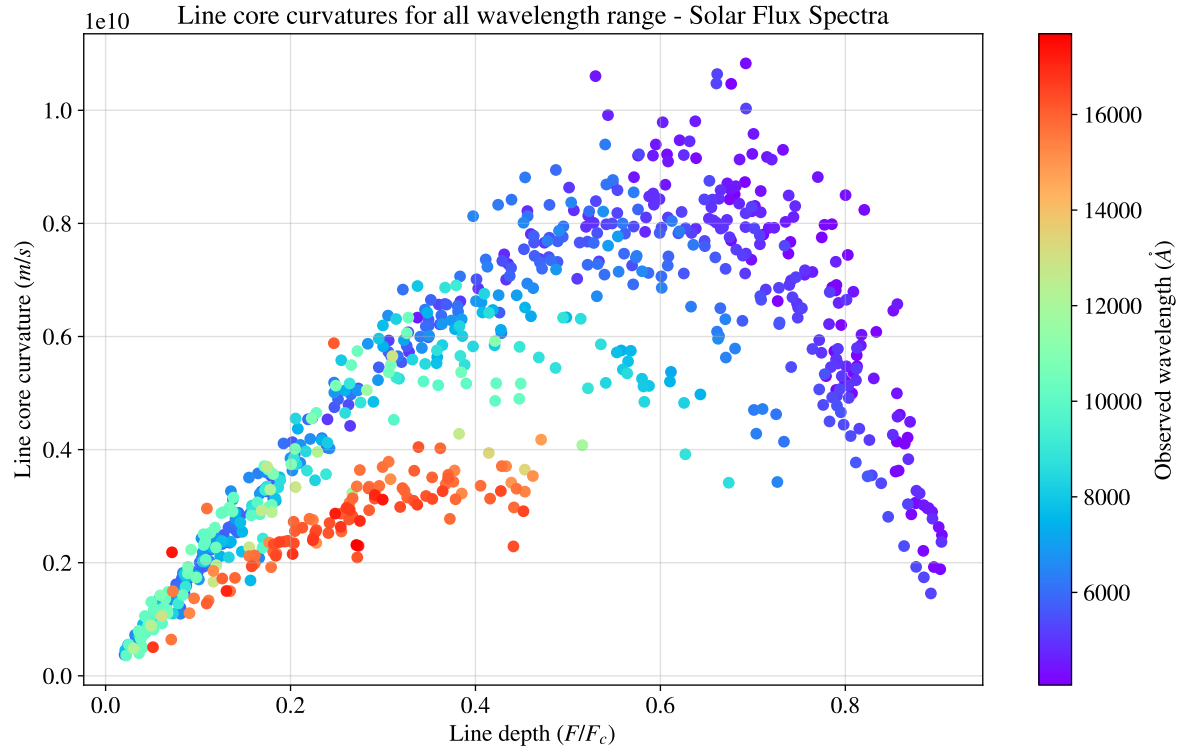


Figure 4.2: Line core curvature in the Solar Flux Atlas. The near infrared range presents a natural division due telluric lines in the atmosphere.

Despite the line depth-dependent shifts along wavelength, the visible range of the atlas exhibits a clear linear tendency (see figure 4.2). Consequently, a first order polynomial fit was applied to the data in the range  $(0.0 - 0.1)F/F_c$  of line depth of the Solar Flux Atlas, where  $F/F_c$  represents the normalized flux.

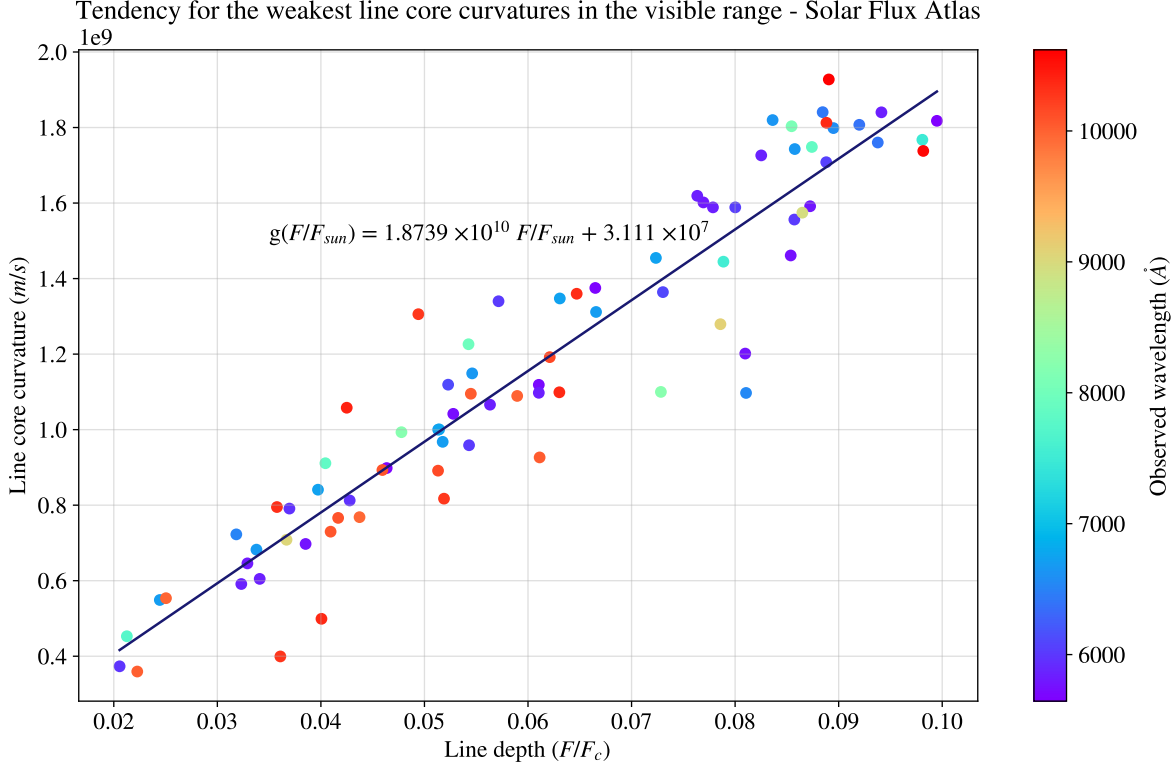


Figure 4.3: Linear polynomial fit applied to the range  $(0.0 - 0.1)F/F_c$  of line depth in the visible range of the Solar Flux Atlas.

As shown in Figure 4.3, the slope of the relationship has a value of  $1.8739 \times 10^{10}$ . The absence of chromodependence in this spectral range indicates that line core curvatures have a net dependence on hydrodynamic velocities, with negligible influence from atomic effects. To confirm this statement, the line core curvature was also plotted for the visible range using the Spatially Resolved Quiet Sun Atlas at the solar limb  $\mu = 0$ , as shown figure 4.4. In other words, this analysis uses disk-integrated flux from the center of the solar disk, which is not affected by rotational Doppler broadening, thereby isolating the external effects.

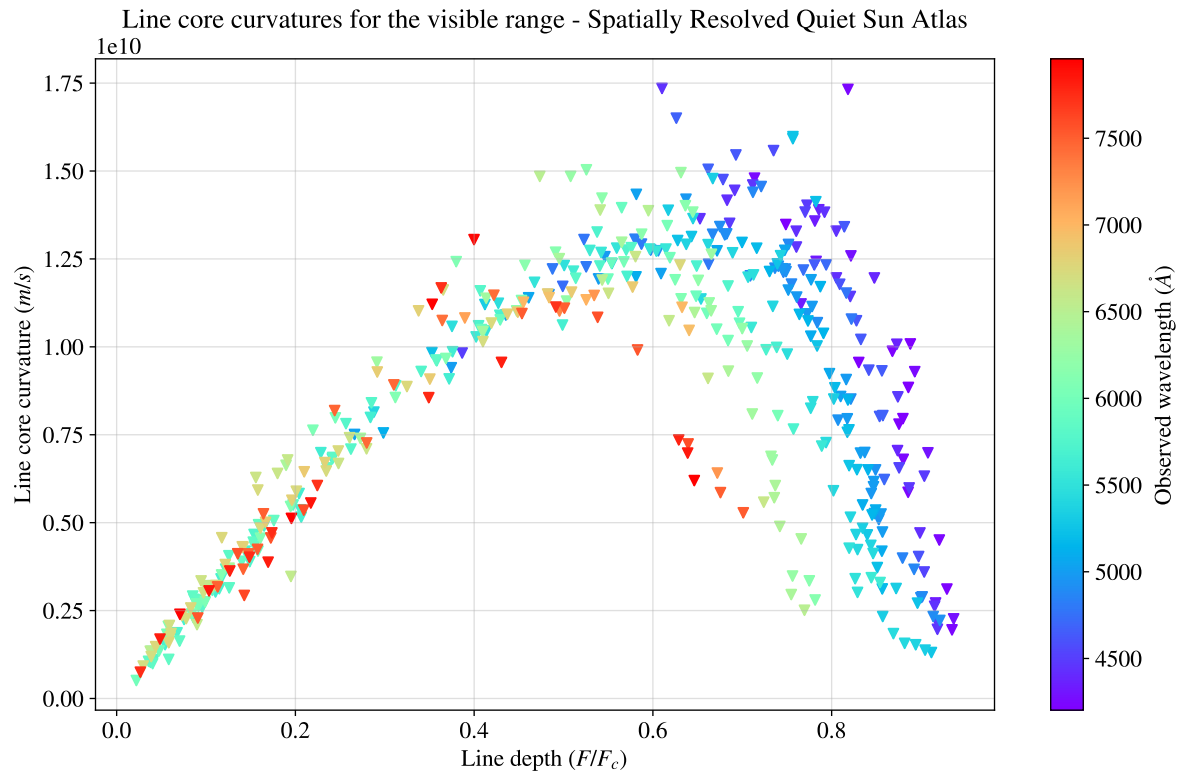


Figure 4.4: Line core curvature for the visible range for disk center data from the Spatially Resolved Quiet Sun Atlas.

A first order polynomial fit in figure 4.5 shows a value of  $2.9360 \times 10^{10}$  for the slope.

Tendency for the weakest line core curvatures in the visible range - Solar Flux Atlas  
1e9

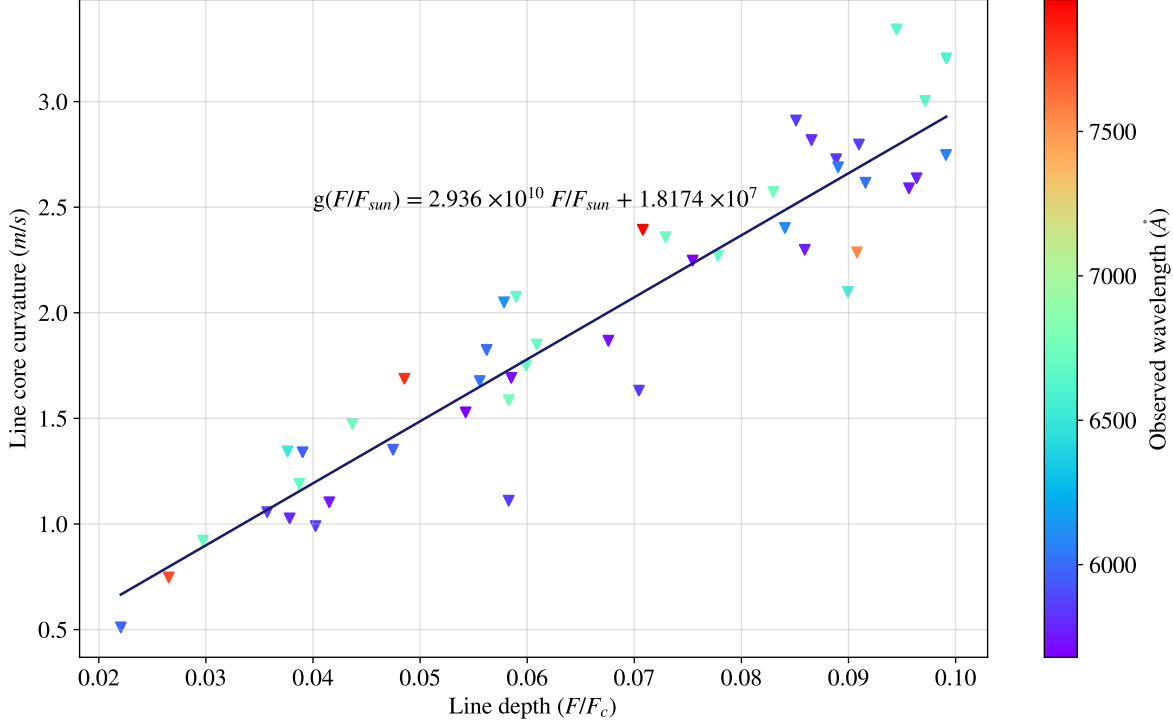


Figure 4.5: First order polynomial fit applied to the range  $(0.0 - 0.1)F/F_c$  of line depth in the visible range of the Spatially Resolved Quiet Sun Atlas.

This result confirms the hypothesis that weaker lines, which have smaller line core curvature, are systematically displaced across the line depth due to rotational Doppler effects. These weaker lines correspond to transitions with lower excitation energies. Consequently, the relationship between line depth and lower excitation potential was analysed.

#### 4.1.2 Line depth-dependence on lower excitation energy

The Nave list for Fe I lines [15] include the values for the highest and the lowest excitation energy. As shown in the figure 4.6 the relative velocity was plotted against lower excitation energy, where it is not clear a strong shift on the velocity.

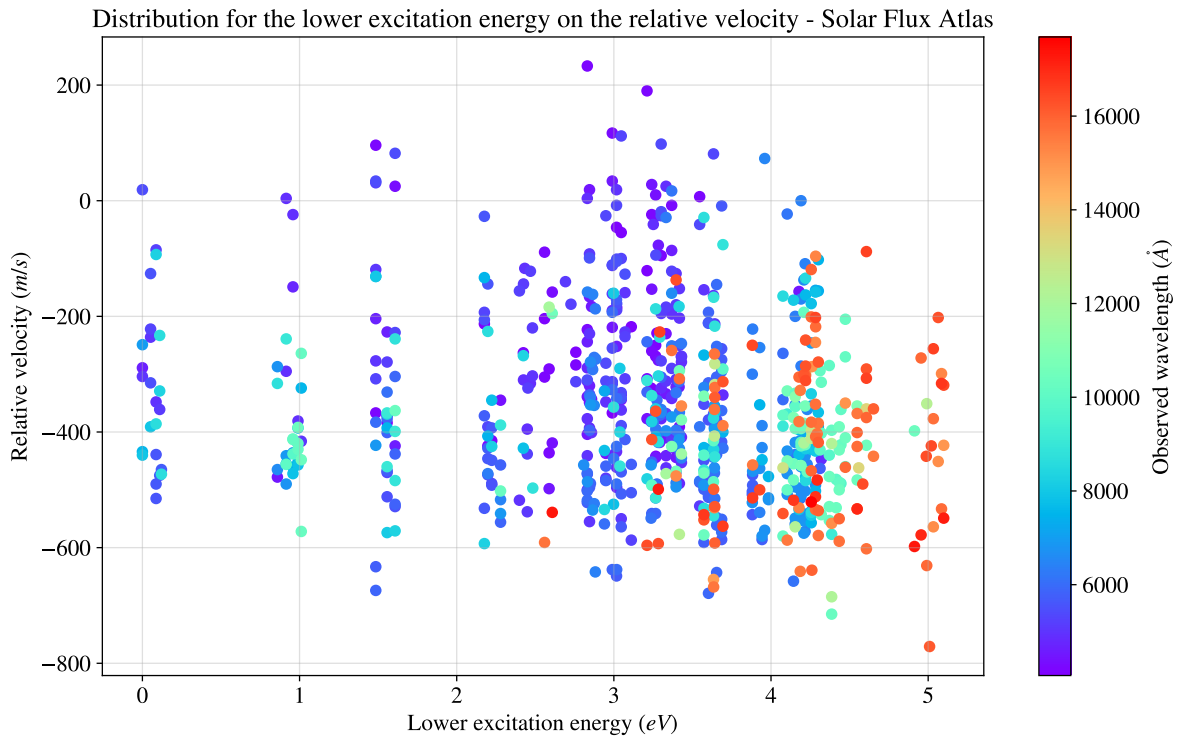


Figure 4.6: Relative velocity against lower excitation energy for all the range in the Solar Flux Atlas

However, if we separate the relative velocity into bins of  $100m/s$  around a fixed velocity and plot lower excitation energy against line depth, shifts in the excitation energy become apparent as shown figure 4.7.

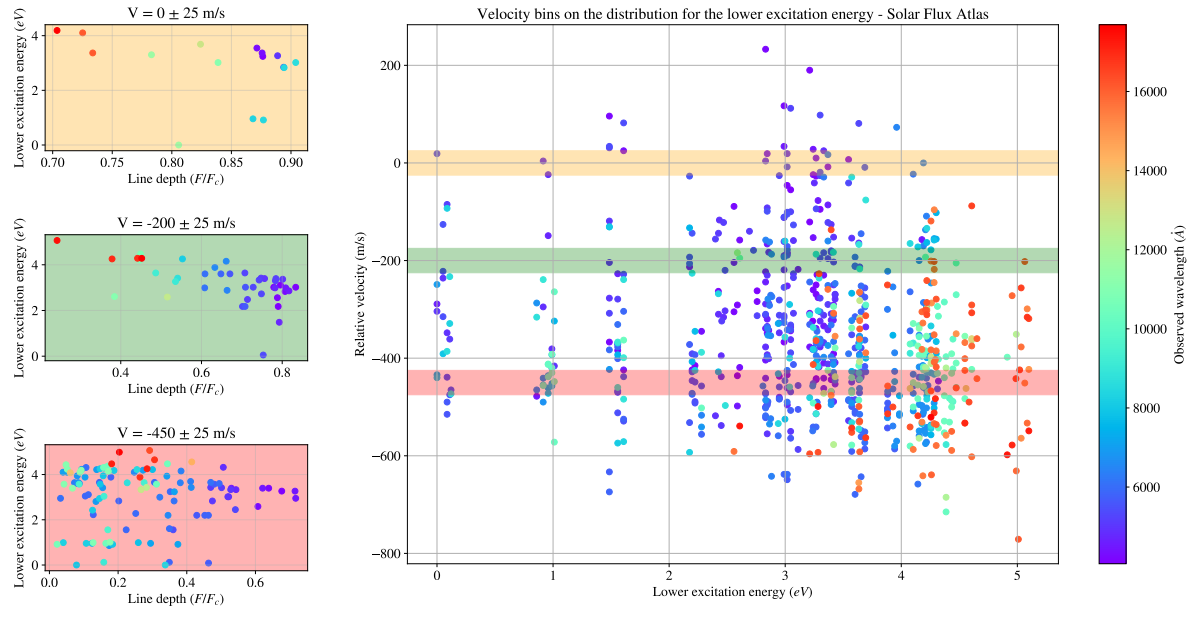


Figure 4.7: Velocity bins of  $100\text{m/s}$  around a fixed velocity, across the figure 4.6, with this separation is visible the energy shift across line depth.

The figure 4.8 explicitly shows the dependency on the highest values for the lowest excitation energy across the wavelength, which can be fitted as a first order polynomial fit.

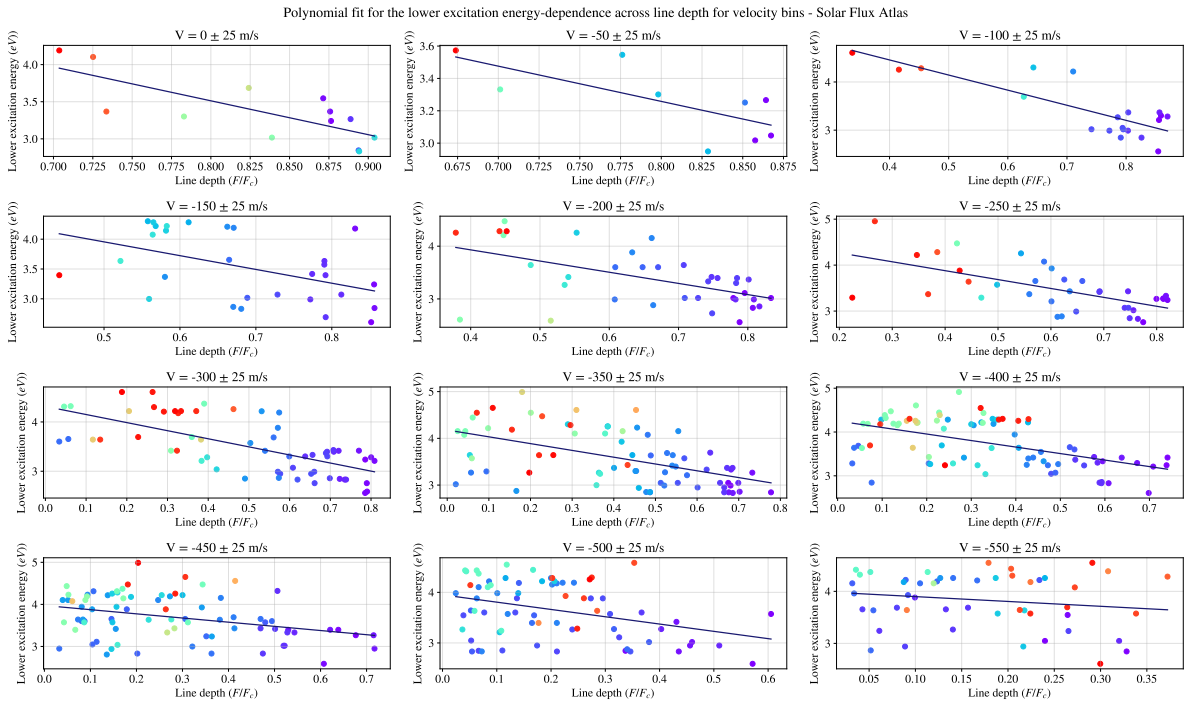


Figure 4.8: Individual plots of lower excitation energy across line depth representing each bin of velocity for the Solar Flux Atlas.

For the velocity range of  $-175\text{m/s}$  to  $-525\text{m/s}$  the calculated slopes are similar, as shown in table 4.1. This indicates a consistent ratio on energy shifts in the energy across the velocity range.

<b>Velocity bin</b>	<b>Shift</b>	<b>Slope</b>	<b>Error slope</b>	<b>Error shift</b>
0	7.1636	-4.5638	1.1564	0.9651
-50	5.0005	-2.1781	0.8069	0.6495
-100	5.7114	-3.1355	0.4958	0.3697
-150	5.1098	-2.3102	0.8208	0.5688
-200	4.7782	-2.1203	0.5594	0.3747
-250	4.6533	-1.9361	0.4121	0.2588
-300	4.3146	-1.6399	0.2408	0.1314
-350	4.1778	-1.4534	0.2694	0.1251
-400	4.2510	-1.4863	0.2683	0.1030
-450	3.9734	-0.9916	0.2973	0.0982
-500	3.9506	-1.4429	0.4428	0.1097
-550	3.9919	-0.9308	0.7750	0.1497

Table 4.1: Values for the first order polynomial coefficients on the different velocity bins for the Solar Flux Atlas.

To corroborate that dependence is only on lower excitation energy, the same analysis was performed on the Spatially Resolved Quiet Sun Atlas at the solar limb  $\mu = 0$ . The plot of relative velocity against lower excitation energy for this atlas exhibits the same qualitative behavior as the Solar Flux Atlas. However, there is a quantitative difference, the first order polynomial coefficients are higher (see figure 4.9 and table 4.2).

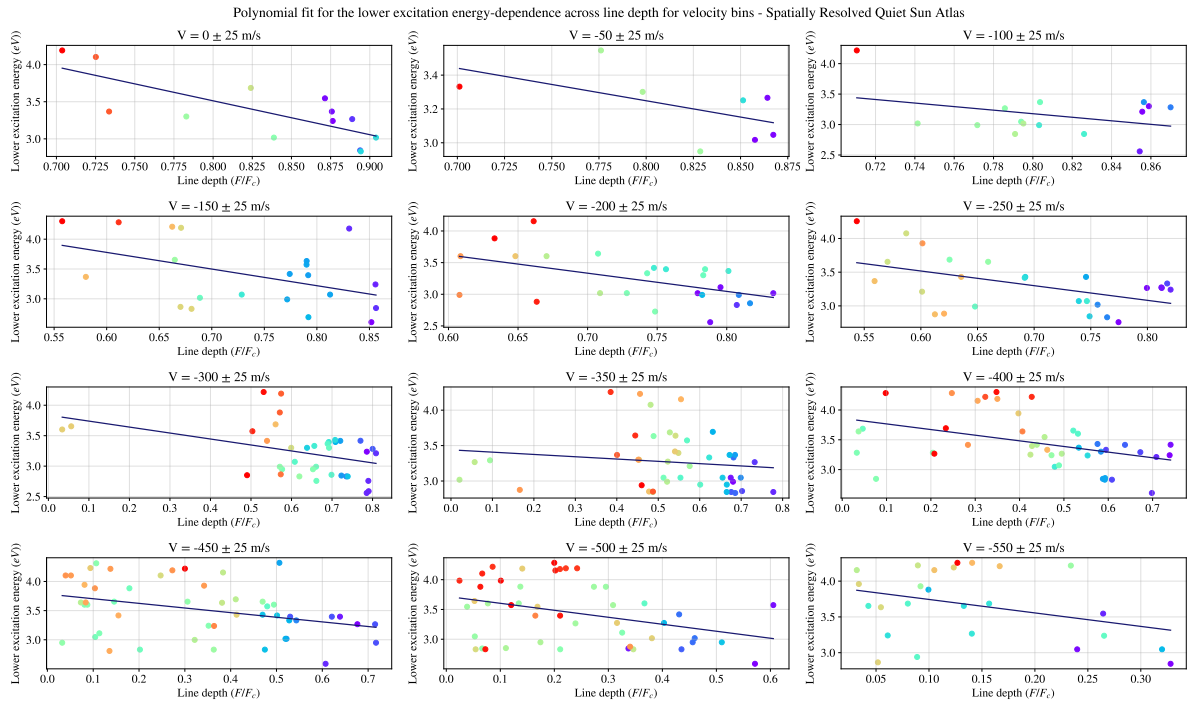


Figure 4.9: Individual plots of lower excitation energy across line depth representing each bin of velocity for the Spatially Resolved Quiet Sun Atlas.

## 4.2 The second signature: Line profile bisector asymmetry

### 4.2.1 The bisector slope

The line core bisector slope was calculated following the equation (2.6) and plotted against line depth, as shown the figure 4.10.

<b>Velocity bin</b>	<b>Shift</b>	<b>Slope</b>	<b>Error slope</b>	<b>Error shift</b>
0	7.1636	-4.5638	1.1564	0.9651
-50	4.7903	-1.9274	1.1583	0.9496
-100	5.5099	-2.9149	2.0695	1.6744
-150	5.4525	-2.7907	1.2421	0.9195
-200	5.3471	-2.8771	0.9840	0.7277
-250	4.8238	-2.1774	0.7516	0.5241
-300	3.8374	-0.9802	0.3714	0.2419
-350	3.4399	-0.3246	0.3473	0.1931
-400	3.8607	-0.9455	0.3184	0.1511
-450	3.7832	-0.7942	0.3032	0.1174
-500	3.7206	-1.1728	0.4614	0.1291
-550	3.9324	-1.8835	1.0826	0.1770

Table 4.2: Values for the first order polynomial coefficients on the different velocity bins for the Spatially Resolved Quiet Sun Atlas.

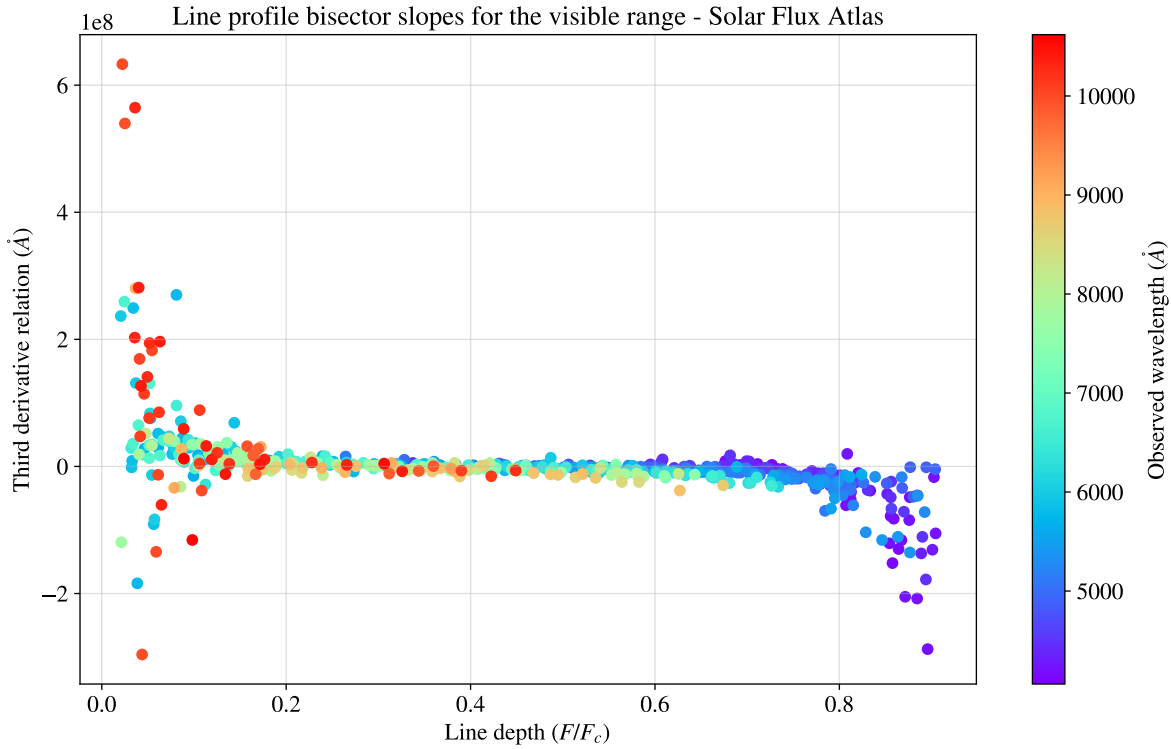


Figure 4.10: Line profile bisector slopes for the visible range in the Solar Flux Atlas. The behavior of the plot is according to the C-curved shape of the line bisector affected by convection movement.

The weakest lines, due to their small depth, do not exhibit a fully developed C-shaped bisector. Instead, their bisectors show as a redshifted slope. In contrast, lines formed deeper in the photosphere experience the convective blueshift in its totality, resulting in a negative bisector slope. The line depths in the middle range represent an equilibrium point where the upward motion of the convective cell is overcome by gravitational forces, leading to overshoot and subsequent descent. Then a first-order polynomial fit was applied to the bisector slope data in the line depth range of  $(0.3 - 0.6)F/F_c$  to quantify this transition, as shown in Figure 4.11.

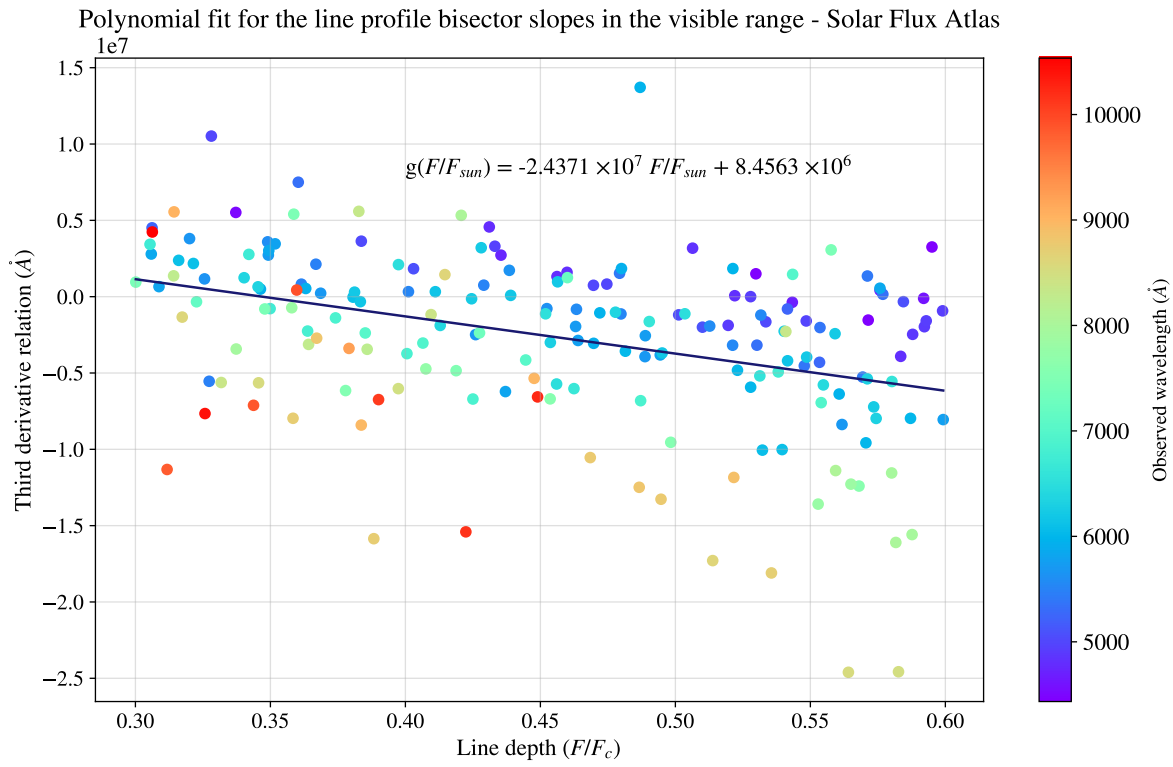


Figure 4.11: First order polynomial fit adjusted to the range  $(0.3–0.6)F/F_c$  for the line bisector slopes.

For a point of comparision, the same analysis was performed to the center limb spectra (see figure 4.12).

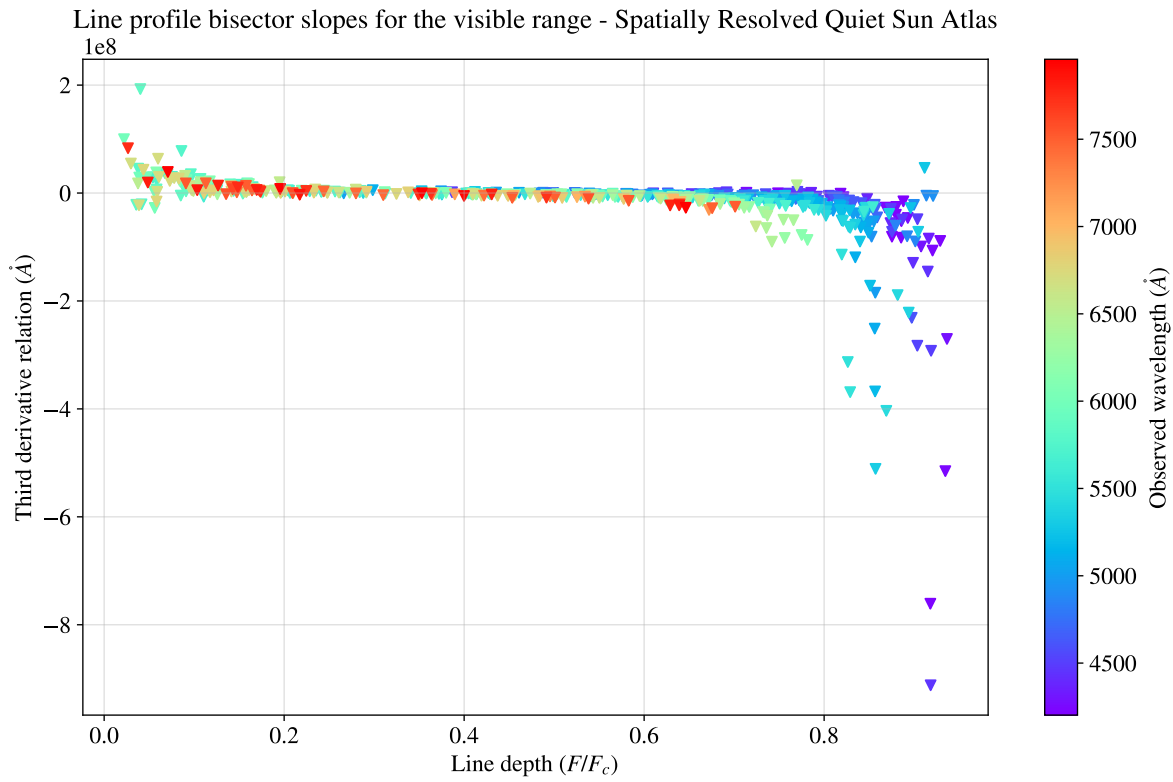


Figure 4.12: Line profile bisector slope for the visible range in the Spatially Resolved Quiet Sun Atlas.

The bisector slope derived from the disk center is smaller in magnitude compared to the integrated flux, despite both exhibiting the same characteristic trend (see Figure 4.13).

Polynomial fit for the line profile bisector slopes in the visible range - Spatially Resolved Quiet Sun Atlas

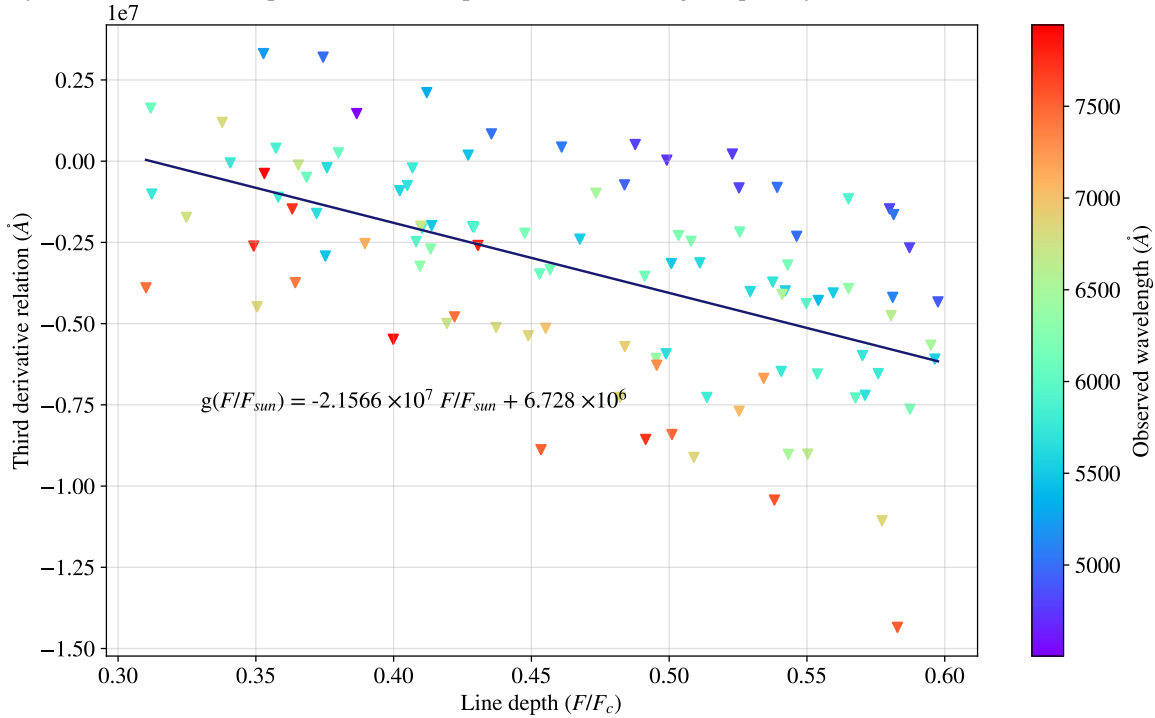


Figure 4.13: First order polynomial fit adjusted to the range  $(0.3–0.6) F/F_c$  for the line bisector slopes.

The phenomenon of chromodependence is presented on the figures 4.11 and 4.13, where the line profile bisectors slopes are organised by decreasing wavelength. This behavior is clearer on the disc center spectra than the integrated flux.

However, if we separate the line depth on bins of 0.1 around a fixed depth and plot the line profile bisector slope against wavelength, shifts in the line bisector slope become apparent as shown figure 4.14.

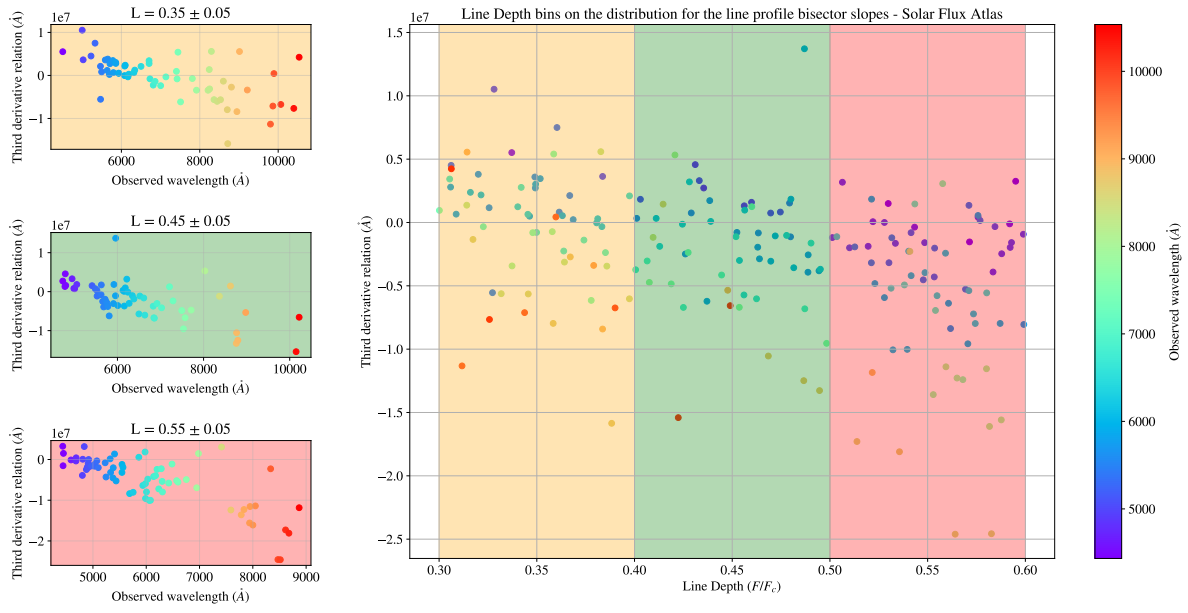


Figure 4.14: Line depth bins of 0.1 around a fixed depth, with this separation is visible the line bisector slope shift across wavelength.

For the integrated flux spectra was found negative slopes with a wavelength dependence (see figure 4.15).

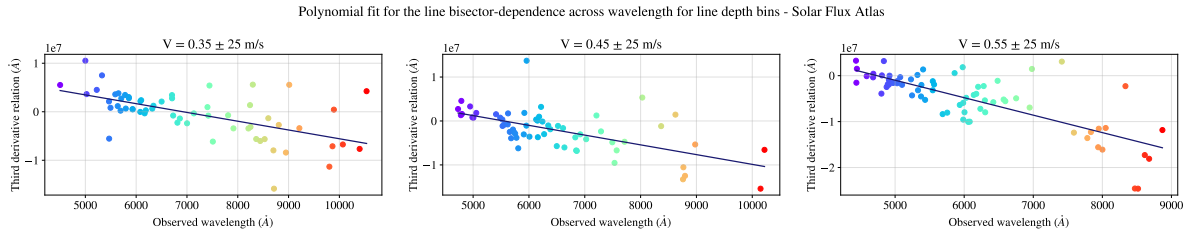


Figure 4.15: Individual plots of line bisector slope shift across wavelength representing each bin of line depth for the Solar Flux Atlas.

The same analysis was performed on the disc center flux and was found the same behavior (see figure 4.16)

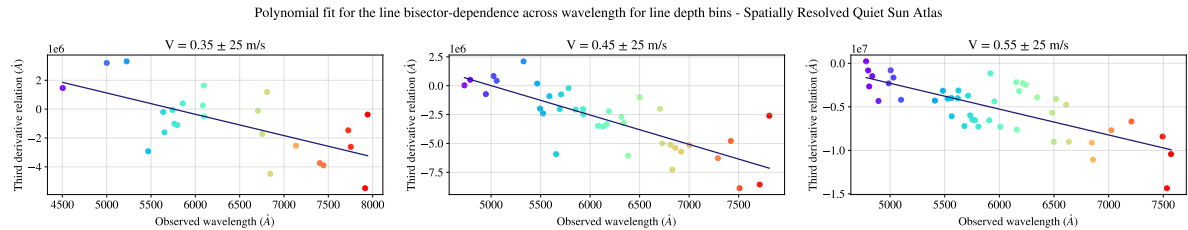


Figure 4.16: Individual plots of line bisector slope shift across wavelength representing each bin of line depth for the Spatially Resolved Quiet Sun Atlas.

#### 4.2.2 Flux deficit (in progress)

Due to radiation, the redshift part of a line is displaced on the flux, inducing a rotation on the c-curved profile bisector. This phenomenon is called flux deficit. Hamilton and Lester [9] noticed that the behavior of the third signature mimics the bisectors gives the sight of the mean bisectors following the granulation pattern behavior, this last is discussed in the next section. Later, Gray and Oostra [7] show that the bisectors need to follow the granulation pattern as the form of we calculated velocities and bisectors.

For comparision with Gray and Oostra work, was taken the line  $6254.2850\text{\AA}$  as shown in figure 4.17.

C-curved bisector for 6254.2850 $\text{\AA}$  in the visible range - Solar Flux Atlas

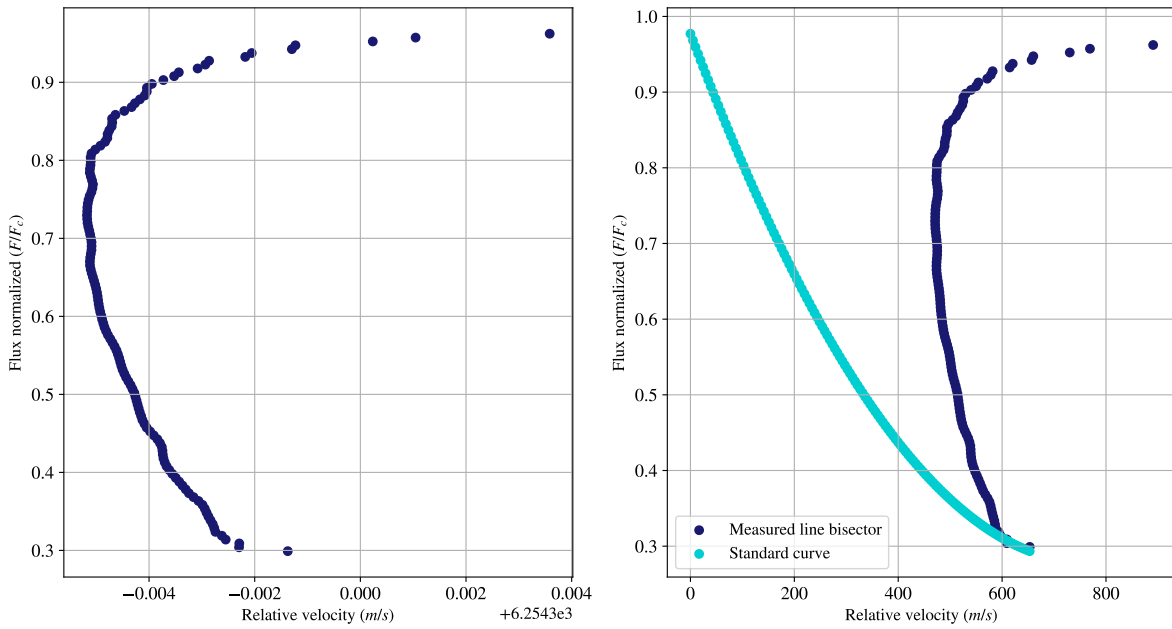


Figure 4.17: C-curved line profile bisector for the 6254.2850 $\text{\AA}$  and the standard curve for the green range from the third signature plot.

Following the same method, the figure 4.18 shows a flux imbalance described on the distribution and temperatures of the mean, the maximum and the RMS point of the bisector.

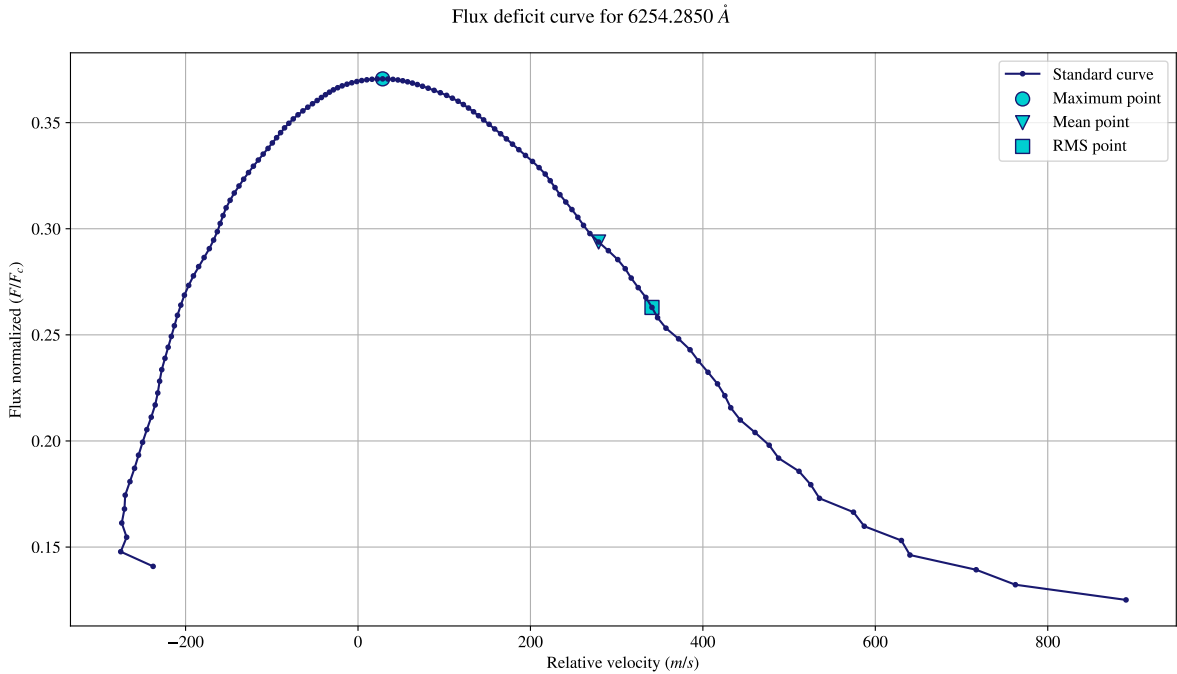


Figure 4.18: Flux deficit curve for the  $6254.2850\text{\AA}$  and the temperatures of the mean, the maximum and the RMS point of the bisector.

The idea is add the flux deficit using the color curves and just report the velocities with the percent of the line corresponds that velocity. As we found the standard curves for all the ranges, the same analysis was realized for a random line in the range of the respective standard curve (im working on that).

## 4.3 The third signature: Line depth-dependence on wavelength shifts

### 4.3.1 The granulation pattern

The granulation patterns for the IAG Solar Flux Atlas in all the wavelength range was obtained.

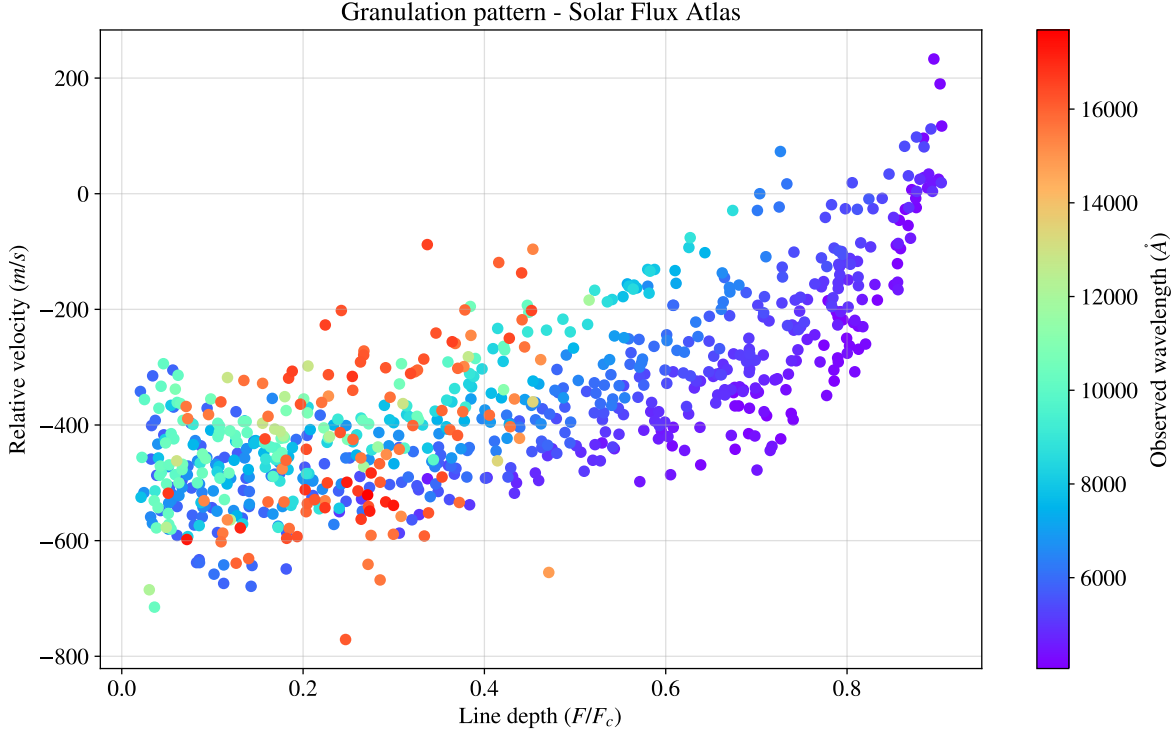
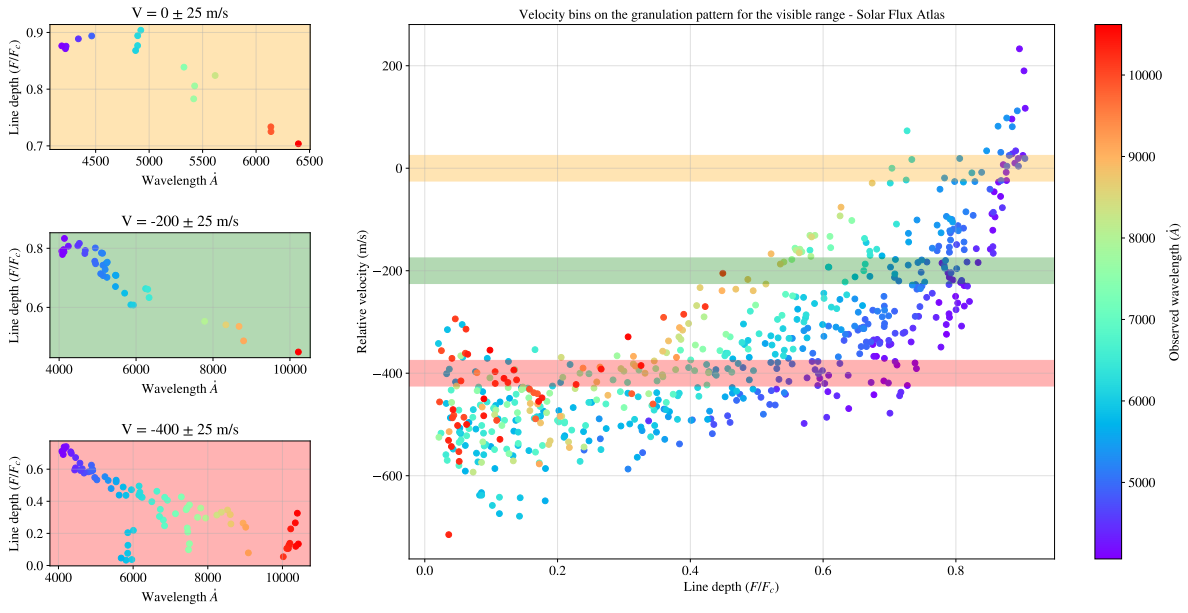


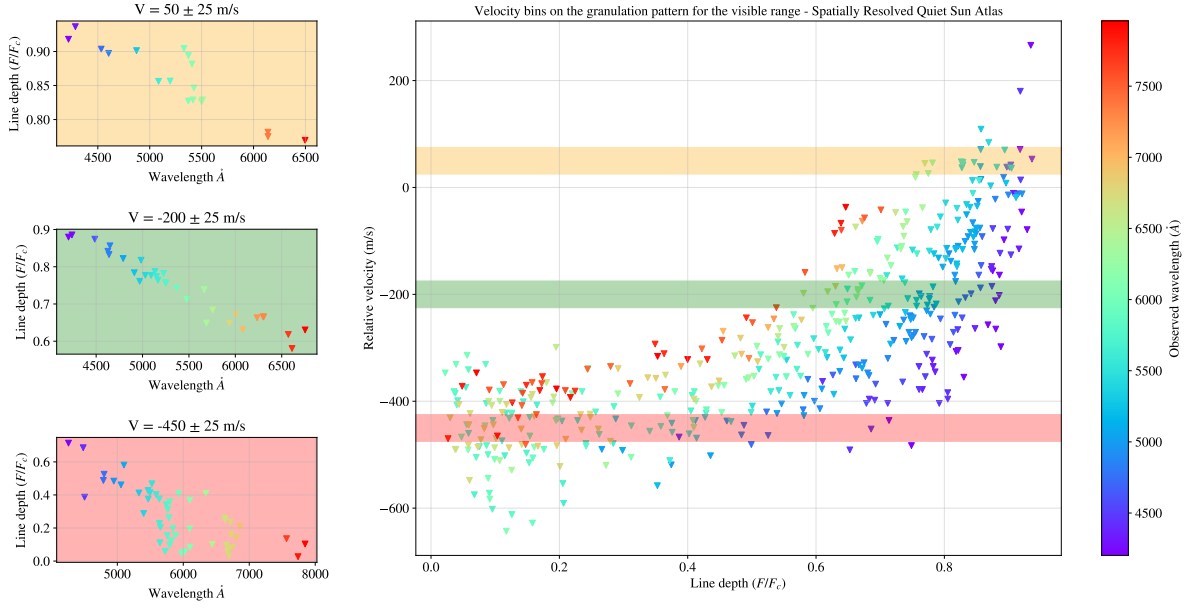
Figure 4.19: Granulation pattern obtained for the Solar Flux Atlas. The wavelength shift dependence is along the line depth.

As shown in Figure 4.19, the behavior along line depth is according to literature, clearly demonstrating the line depth-dependent wavelength shift, also known as chromodependence. To further characterize this trend, an analysis of line depth versus wavelength was performed. The guiding hypothesis was: “If the velocity shift is present only in the disk-integrated Solar Flux Atlas and absent at the disk center, then solar rotation is the cause.” However, the velocity shift was observed in both spectral datasets. This was initially unexpected, as rotational doppler broadening is negligible at the disk center.

To measure these wavelength shifts, the analysis was restricted to the spectral range from  $4300\text{\AA}$  to  $5600\text{\AA}$ . The wavelengths from both atlases were then sorted into velocity bins of  $50\text{m/s}$  (see figure 4.20).



(a) Visible range for the Solar Flux Atlas.



(b) Visible range for the Spatially Resolved Quiet Sun Atlas.

Figure 4.20: Comparision between atlases with velocity bins for the relation between wavelength and line depth. For each velocity bin was plotted wavelength against line depth to measure a frequency shift with a first order polynomial fit.

For each velocity bin was plotted wavelength against line depth to measure a frequency shift

with a first order polynomial fit (see figure 4.21)

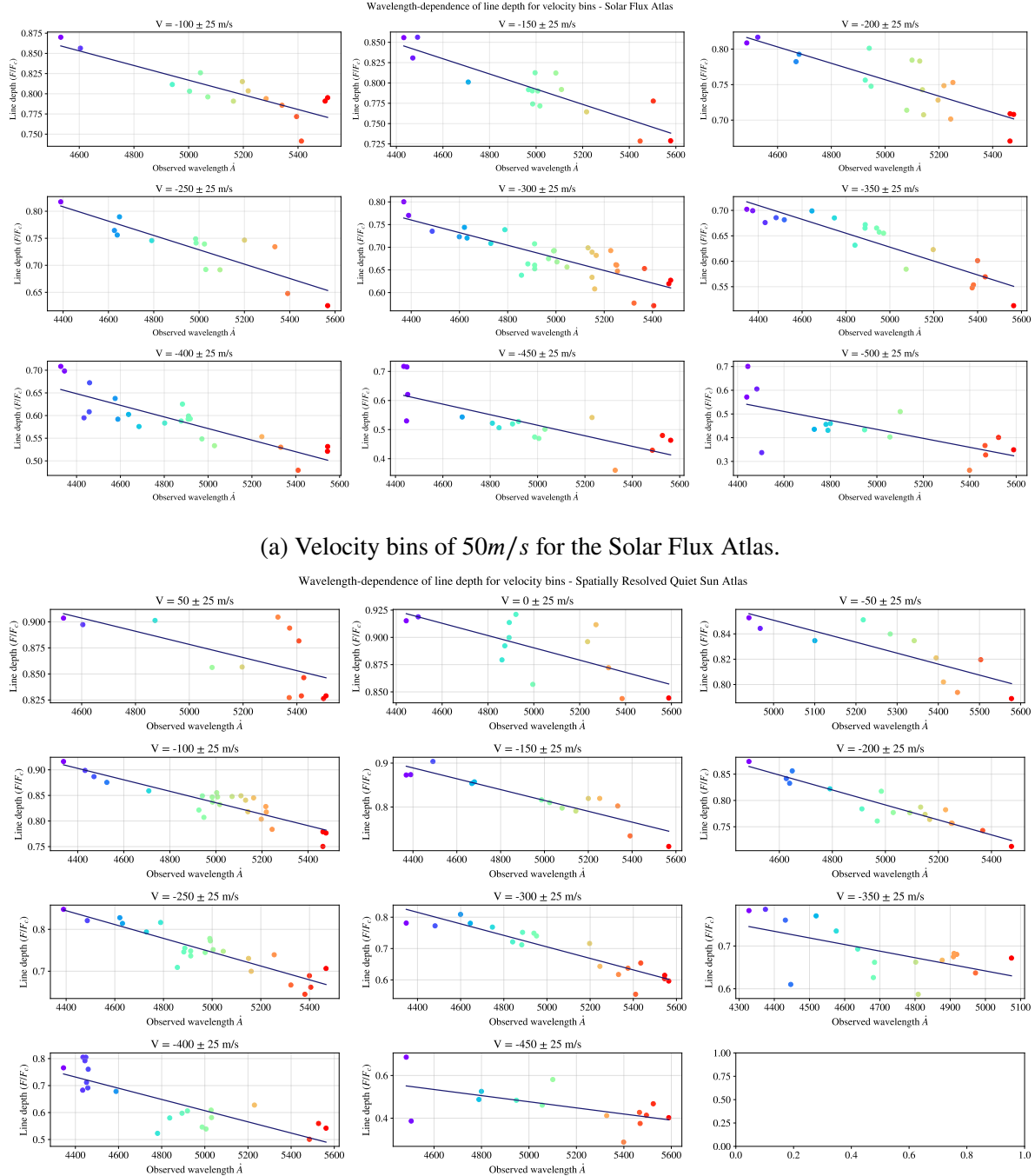


Figure 4.21: Individual plots of lower excitation energy across line depth representing each bin of velocity.

The tables 4.3 and 4.4 shows the obtained slopes in both atlases.

<b>Velocity bin</b>	<b>Shift</b>	<b>Slope</b>	<b>Error slope</b>	<b>Error shift</b>
50	1.1937	-0.000063	0.000022	0.1166
0	1.1720	-0.000056	0.000018	0.0923
-50	1.2840	-0.000087	0.000021	0.1087
-100	1.3953	-0.000112	0.000012	0.0584
-150	1.4327	-0.000124	0.000017	0.0842
-200	1.5028	-0.000142	0.000013	0.0658
-250	1.5712	-0.000165	0.000018	0.0890
-300	1.6233	-0.000184	0.000019	0.0971
-350	1.4129	-0.000154	0.000055	0.2583
-400	1.6455	-0.000208	0.000033	0.1617
-450	1.1952	-0.000144	0.000060	0.3094

Table 4.3: Slopes for the first order polynomial fit in each velocity bin for the Spatially Resolved Quiet Sun Atlas.

<b>Velocity bin</b>	<b>Shift</b>	<b>Slope</b>	<b>Error slope</b>	<b>Error shift</b>
-100	1.2704	-0.000091	0.000015	0.0797
-150	1.2601	-0.000094	0.000013	0.0673
-200	1.3340	-0.000115	0.000019	0.0985
-250	1.3920	-0.000133	0.000023	0.1164
-300	1.3724	-0.000139	0.000017	0.0874
-350	1.3106	-0.000137	0.000015	0.0744
-400	1.2119	-0.000128	0.000018	0.0866
-450	1.4212	-0.000181	0.000039	0.1947
-500	1.3787	-0.000189	0.000052	0.2609

Table 4.4: Slopes for the first order polynomial fit in each velocity bin for the Solar Flux Atlas.

The value of slopes for the Spatially Resolved Quiet Sun Atlas are greater than the Solar Flux Atlas, which contradicts the initial hypothesis.

### 4.3.2 Characterization of chromodependence on granulation pattern

The figure 4.22 show the standard curve proposed for Gray and Oostra [7], established on the range  $6020 - 6340\text{\AA}$

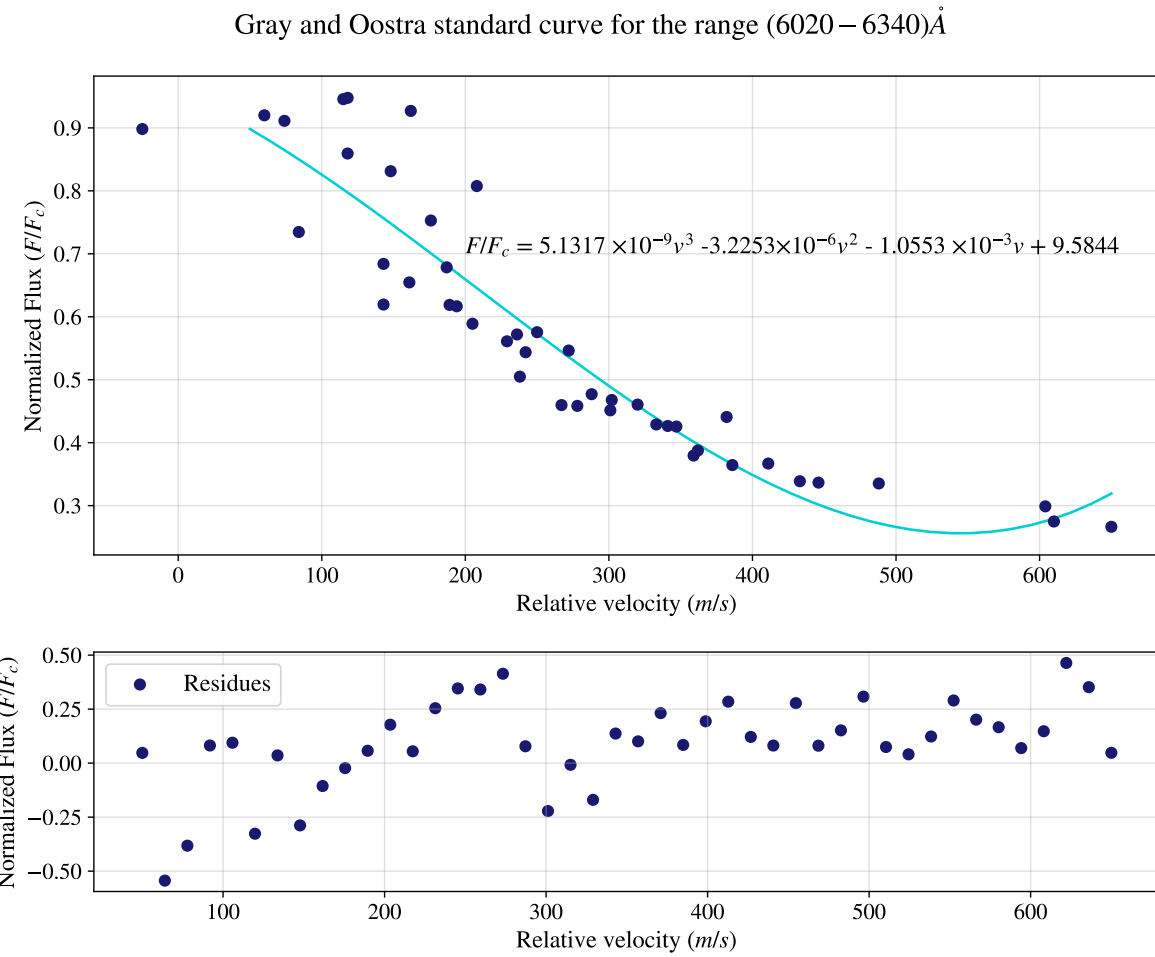


Figure 4.22: Standard curve given by Gray and Oostra and recalculated for comparison with the current work.

Since the standard curve does not account for the full wavelength range and the given third-order polynomial fit overestimates the data points, a different approach was adopted. The

spectrum was separated into distinct color ranges, and a second-order polynomial was fitted to each segment.

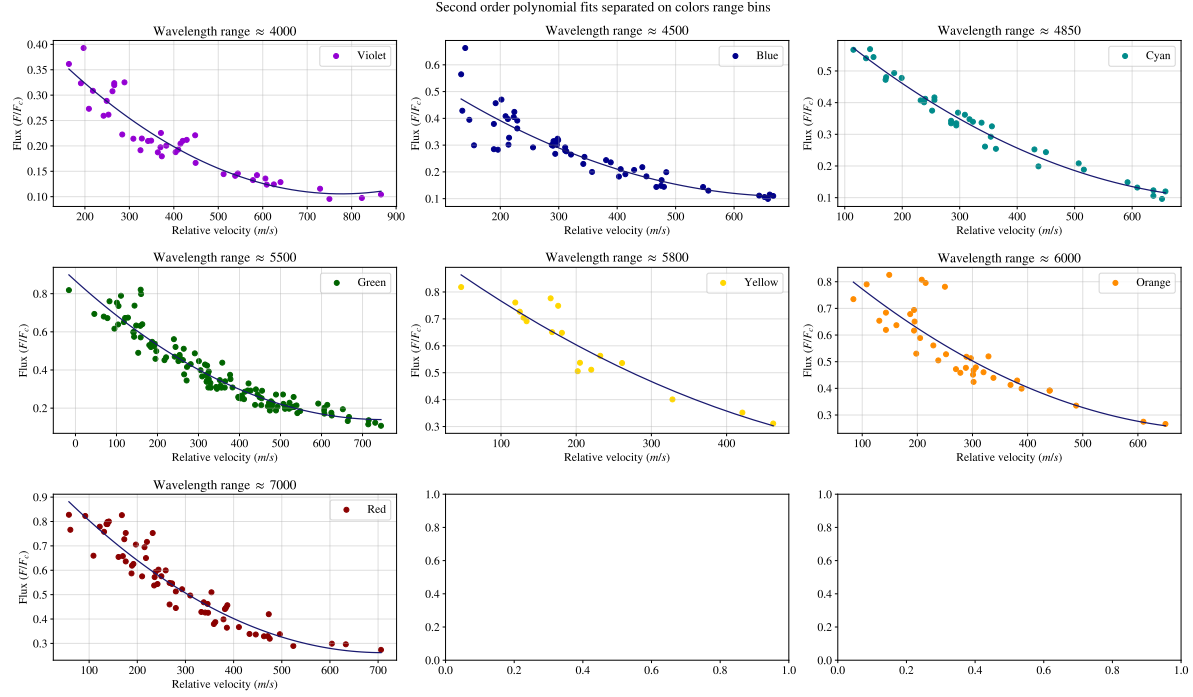


Figure 4.23: Different color curves fitted to a specific range on granulation pattern for the visible range in the Solar Flux Atlas. The tendency on the curves is more pronounced in the violet and red range.

The trend in the curves is more pronounced in the violet and red ranges. This can be interpreted as a shift and flattening of the standard curve from Gray and Oostra towards shorter wavelengths. Using the curve for the range  $4970\text{--}5700\text{\AA}$  as a reference (green standard curve), distinct scaling coefficients were calculated for each color segment, as shown in Table 4.5.

Wavelength range ( $\text{\AA}$ )	Color coefficient
3800-4270	0.5359
4270-4760	0.8195
4760-4970	0.8348
4970-5700	1.000
5700-5810	1.0595
5810-6180	0.9834
6180-7800	1.1149

Table 4.5: Scaling factors  $\alpha_c$  to the new standard curve shown in the equation (4.1).

The equation (4.1) reports a new, color dependent standard curve. Its coefficients ( $\alpha_c$ ) vary with the color range, generating the corresponding granulation pattern for each spectral segment listed in Table 4.5.

$$F/F_c = \alpha_c(1.2925 \times 10^{-6}v^2 - 0.0019v + 0.8671) \quad (4.1)$$

However, when the color coefficients  $\alpha_c$  are plotted against wavelength, they exhibit a quadratic tendency that increases with longer wavelengths. This finding leads us to model the coefficient  $\alpha_c$  as a function of wavelength, as shown in equation (4.2)

$$\circledast(\lambda) = -6.7598 \times 10^{-8}\lambda^2 + 9.1584 \times 10^{-4}\lambda - 2.0041 \quad (4.2)$$

Then, the characterization for the granulation pattern it can be described by equation 4.3

$$F/F_c(\lambda, v) = \circledast(\lambda)[1.2925 \times 10^{-6}v^2 - 0.0019v + 0.8671] \quad (4.3)$$

On the other hand, chromodependence was also identified in the near infrared range, although it is less pronounced than in the visible spectrum. There were defined specific wavelength ranges by excluding regions dominated by telluric absorption lines, and was found linear relationships for each range (see Figure 4.24). However, unlike the visible range these relationships do not exhibit a unified correlation.

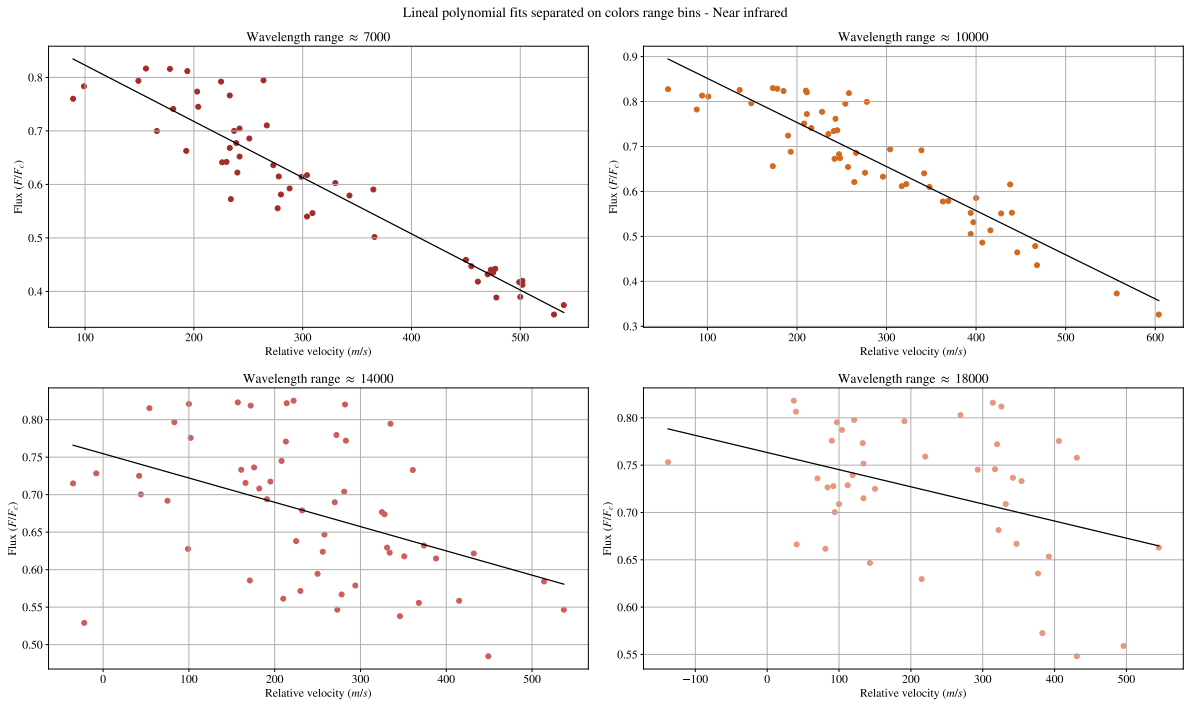


Figure 4.24: Different color curves fitted to a specific ranges on granulation pattern for the near infrared range in the Solar Flux Atlas.

The coefficients for each linear fit applied are shown in the table 4.6.

<b>Wavelength range</b>	<b>Slope</b>	<b>Shift</b>
7000-8500	-0.0010	0.9279
8500-11000	-0.0009	0.9496
11000-16000	-0.0003	0.7546
16000-23000	-0.0001	0.7633

Table 4.6: Coefficients for the first order polynomial fit in each wavelength range in the near infrared.

## 4.4 Higher quality graphs

To show the improvement on the quality in the third signature plots, the figure 4.25 compare the plot obtained by Ellwarth [6] and the granulation pattern obtained in this project.

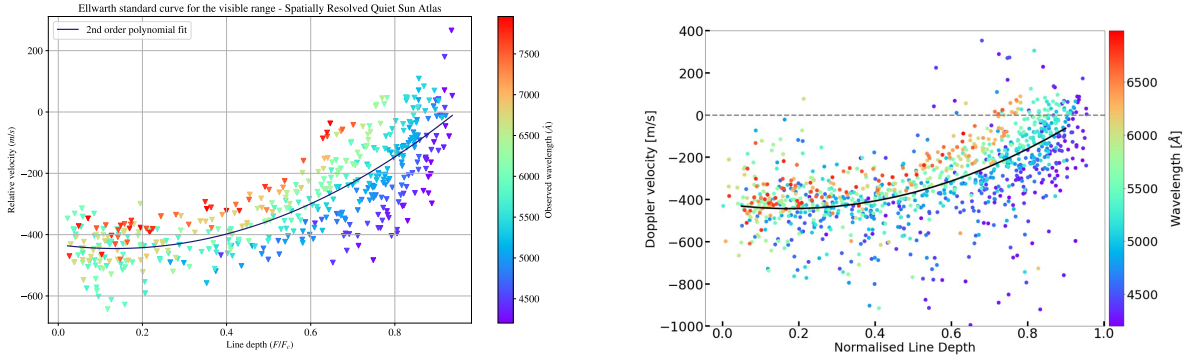
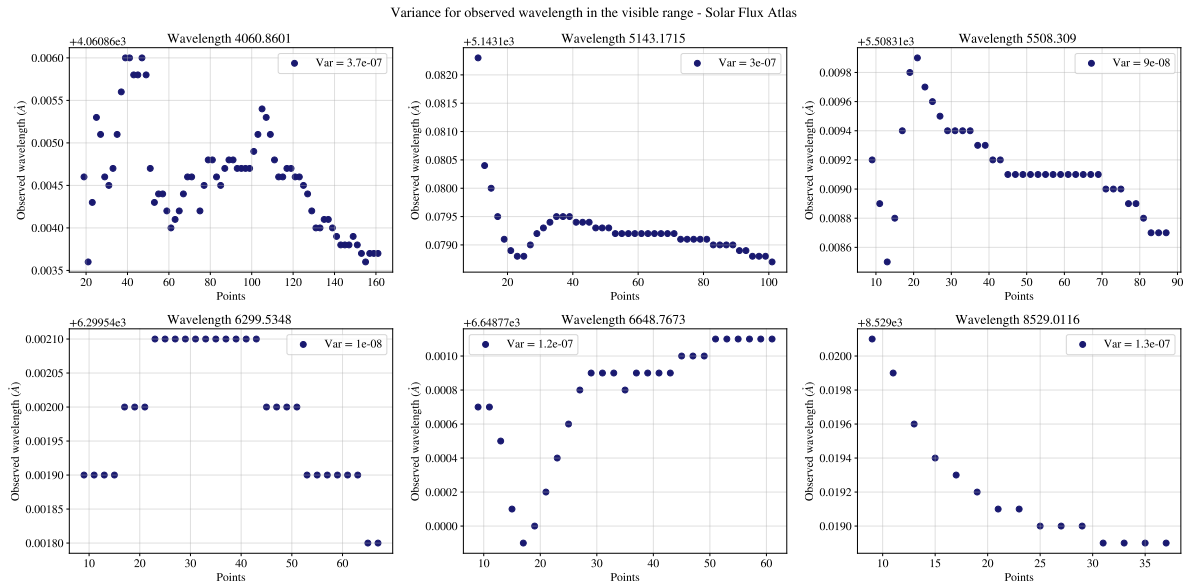
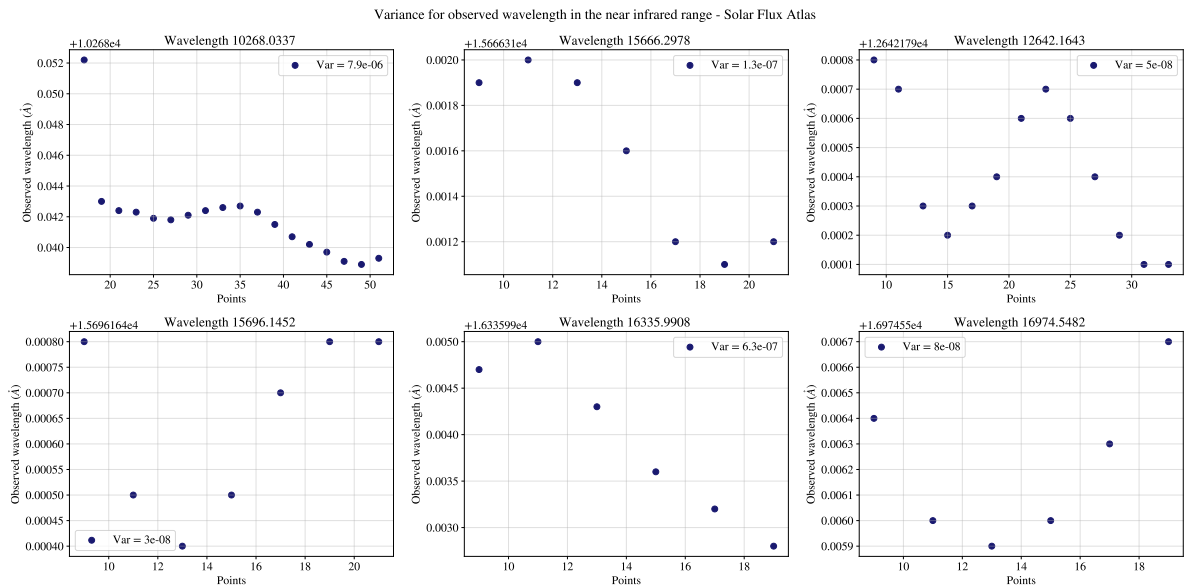


Figure 4.25: We realized the same graphic for the comparision with the Ellwarth article to show the less scattered points.

The less scattered points and the improvement on the chromodepence identification is evident. Furthermore, the variance of the observed wavelength was analyzed by altering the number of points used in the fourth-order polynomial fit. Figure 4.26 shows that this parameter set performs well in the visible spectrum. However, its performance degrades in the infrared, where the number of data points defining the line core is reduced compared to a typical line in the visible range.



(a) Variance for random lines in the visible range for the Solar Flux Atlas.



(b) Variance for random lines in the near infrared range for the Solar Flux Atlas.

Figure 4.26: Variance of the observed wavelength altering the number of points on the fourth order polynomial fit

# **Chapter 5**

## **Conclusions**

In conclusion, this project characterized the convective blueshift in solar absorption lines and its dependence on both line depth and wavelength range.

Specifically, was produced a refined, blend-free list of Fe I lines and derived solar granulation patterns with minimal scatter. Also provided a detailed description of how the granulation pattern varies with wavelength, establishing a new, color-dependent standard curve.

(In progress..)

# Appendix A

## Z-score Standardization

In the process of calculating the fourth-order polynomial fit the function `np.polyfit()` presents an over estimation on the coefficients, due to the large difference of magnitude order between axes. To deal with this difference a z-score standardization was used on the selected bins of wavelengths around the reference point for a minimum. This process helps to avoid the dominance of certain features over others due to differences in their scales [17].

The follow up for the standardization was applied the relation (A.1) on the selected bins for wavelength.

$$\lambda_{scaled} = \frac{\lambda_{original} - \mu(\lambda_{original})}{\sigma(\lambda_{original})} \quad (\text{A.1})$$

Where  $\mu(\lambda_{original})$  refers to the mean and  $\sigma(\lambda_{original})$  to the standard deviation of the wavelength range. As the wavelength was scaled, in terms of calculated derivatives for the first and the second signature, a re-scaled for these values was necessary. Based on the definition for the standardization, the derivatives follow the relation (A.2).

$$\frac{d}{d\lambda_{original}} = \frac{1}{\sigma(\lambda_{original})} \frac{d}{d\lambda_{scaled}} \quad (\text{A.2})$$

Taking the derivative of the expression (A.1) a factor related to the standard deviation appears. With this, the original values for derivatives evaluated in the observed wavelength are expressed in equation (A.3)

$$\frac{d^2}{d\lambda_{original}^2} = \frac{1}{\sigma(\lambda_{original})^2} \frac{d^2}{d\lambda_{scaled}^2} \quad \quad \quad \frac{d^3}{d\lambda_{original}^3} = \frac{1}{\sigma(\lambda_{original})^3} \frac{d^3}{d\lambda_{scaled}^3} \quad \quad \text{(A.3)}$$

This improved considerably the precision in the fit and there over the precision on the observed wavelength calculated.

# Appendix B

## The third derivate relation

The third derivate relation or called the line profile bisector slope was deducted by Professor Benjamin and showed below.

We defined the slope as equation (B.1), where the points  $b, c, h$  are illustrated in the figure ??

$$CBS = \lim_{h \rightarrow 0} \frac{\frac{b+c}{2} - a}{h} \quad (\text{B.1})$$

Note that in a symmetrical line the bisector is vertical and the slope, according to this definition, is zero. Now, the curve may be expanded around the point  $a$  by Taylor series noticing that  $a$  is chosen at the minimum, so  $f'(a) = 0$  and  $f(c) - f(a) = h$ , giving

$$2h = (c - a)^2 f''(a) + \frac{1}{3}(c - a)^3 f'''(a) \quad (\text{B.2})$$

We may abbreviate  $c - a = x > 0$  and likewise  $b - a = y < 0$  obtaining

$$2h = x^2 f''(a) + \frac{1}{3}x^3 f'''(a) \quad 2h = y^2 f''(a) + \frac{1}{3}y^3 f'''(a) \quad (\text{B.3})$$

So,  $x$  and  $y$  are tow equations roots. The core bisector slope is now defined by

$$CBS = \lim_{h \rightarrow 0} \frac{x + y}{2h} \quad (\text{B.4})$$

One of the possible roots for the cubic (ideal 4th order) equation, the two that we need are those that trend to

$$CBS = \lim_{h \rightarrow 0} \frac{x}{y} = -1 \quad (\text{B.5})$$

If wrote the polynomial equation in the standard form  $ax^3 + bx^2 + cx + d = 0$  the coefficients are  $a = \frac{f'''}{3}$ ,  $b = f''$ ,  $c = 0$ ,  $d = -2h$ . A standard procedure id to change variable to  $x = t - \frac{b}{3a} = t - \frac{f''}{f'''}$  which produces the "depressed" equation.

$$t^3 + pt + q = 0 \quad \rightarrow \quad p = -3 \left( \frac{f''}{f'''} \right)^2 \quad q = 2 \frac{(f'')^3 - 3h(f''')^2}{(f''')^3} \quad (\text{B.6})$$

Where the equation have three solutions of the form:

$$t_i = 2 \left( \frac{f''}{f'''} \right) \cos \left( \frac{1}{3} \arccos \left( \frac{3h(f''')^2}{(f'')^3} - 1 \right) - \frac{2\pi i}{3} \right) \quad (\text{B.7})$$

When  $h$  vanishes, there are two equal solutions and one differing. LeTS abbreviate

$$\epsilon = \frac{h(f''')^2}{(f'')^3} \ll 1 \quad (\text{B.8})$$

In the limit  $h \rightarrow 0$  we have  $\epsilon \ll 1$  which means  $\arccos(3\epsilon - 1) = \pi - \delta$  with  $\delta$  an small angle.

So,  $\delta = \sqrt{6\epsilon}$  and the solution that we need

$$t_{\pm} = 2 \frac{f''}{f'''} \left( \frac{1}{2} \cos \left( \frac{\sqrt{6\epsilon}}{3} \right) - / + \frac{\sqrt{3}}{2} \sin \left( \frac{\sqrt{6\epsilon}}{3} \right) \right) \quad (\text{B.9})$$

For the bisector slope we need

$$x + y = t_+ + t_- - 2 \left( \frac{f''}{f'''} \right) = -\frac{2}{3} \left( \frac{f''}{f'''} \right) \epsilon = -2h \frac{f''}{3(f''')^2} \quad (\text{B.10})$$

Whence, finally, the core bisector slope is defined by equation (B.11)

$$CBS = -\frac{f''}{3(f''')^2} \quad (\text{B.11})$$

In the code it was multiplied by the relation  $(\frac{c}{\lambda})$  to see each clear in the graphic.

# **Appendix C**

## **Visualizer for outliers**

For the process of the blend-free list a visualizer was created using the library Tkinter with the objective to help the selection process of outliers. Two versions of the visualizer were created, separated by filters. The first filter only shows the geometry of the line core and the line profile bisector. The second filter, which uses the selected lines for the first one, shows the three signatures of convection and the behavior of the selected line in each one.

Thanks to this visualizer the time expended seeing lines was reduced significantly. Specially cause count with his own system to classification, adding lines to a Dataframe and save the images. Following the motivation this can be seen on [GitHub](#) and it's given a test example below.

REMEMBER: The window for the abs in the local minimums points are 0.01A

### **C.1 Test example**

The main code is in the file Visualizer.ipynb and the test example data are test.xlsx, feel free to change the type of data, the important is make a dataframe where the columns are [Wave , Flux] wavelength on Armstrong and flux normalized preferred. Then made another dataframe with the list of lines of Fe I.

Use the function closer lines to select the closer minimums of the Fe I lines, with the flux and Fe I line associated. Don't be confused, this is not the observed wavelength. This point is a

reference for selecting the bins around the Fe I line. The function discards distances between minimums and Fe I line over  $0.001\text{\AA}$ . Furthermore, assuming the statement that fourth order polynomial fits need to be convex, were discarded fits with the second order coefficient negative and equal to cero. For discarding the lines which don't belong to the spectrum an approximation was taken. A computational form of a slope can be seen as the difference between the maximum and minimum point of the list of points. In terms of flux if it is seen the distance can't be more than a half of the absolute difference. This lets us discard pronounced slopes without affecting or filtering weaker lines. Then use the function local points for selecting the bins of  $0.1m\text{\AA}$  around the minimal point, each corresponding to one index on the closer lines dataframe.

If it runs correctly, the graphics for the intervals (), (), and () need to be seen like figure (). The next function Fit Derivatives finds the fourth order polynomial fit and calculates the minimum point with the second derivative of the fit, that is the observed wavelength. This returns a dataframe with the Fe I line associated, the polynomial fit, and the observed wavelength. In parallel is calculated the bisectors of each line following the midpoint method, where equal points of flux are selected for comparison.

With this information can be used the first visualizer

From this is the first visualizer that receives the local points, the values and the fit. This shows the line core and the fourth polynomial fit, in parallel is shown the bisector of each line in terms of velocity.

We recommend eliminating the lines that follow one of the conditions presented below: 1)The bisector doesn't show a C-curved bisector or it's too affected by the noise. 2)There is no curve or polynomial fit. This can be interpreted as the position on other points to the fit. 3) There's too much noise on the original line.

With this first filter the number of possible lines are reduced for calculating derivatives.

The second part of the code calculates the granulation pattern, core curvature and bisector slope. With these values the visualizer shows all the graphics including the line profile with the polynomial fit. In each graphic of derivatives the corresponding Fe I is resalted, this with the finally to select lines depending on his behavior.

This is a code test: Run the file test, you can adapt this part on your necessities. The idea is the Dataframe results have the columns Wave (cm), nFlux and Wave A (there's no need for the flux to be normalized, it cannot be, we test this on arturus).

Then run the nave list, the present github has the table organized on an excel.

Run the cell of closer points and local points, the first needs to be returned a Dataframe and the other a list of dataframes.

For the first filter code you need to have a dataframe with the columns (), the list of local points and the closer lines associated with the Dataframe, the fit values and the covariance values.

Modified this line to call the first visualizer.

Then, this part helps to extract the Dataframe with the lines that don't behave like the condition parameters. This can also help to drop the unnecessary lines

For the second enter the file with the lines resulting in the first filter, and run again the code for closer lines and local points, and then the second big filter.

Modified this line to call the second visualizer.

The next line helps to extract the lines to drop and remove it for the Dataframe.

## C.2 Conditions justifications

Two is for observations on polynomial fits that derive for mathematics properties. The third born on the many observations that i realize after the creation of visualizer, I see the parameter of 0.001 for near lines and I put the value

# Bibliography

- [1] P. Eric, *Solar magnetohydrodynamics*. Kluwer, 1982.
- [2] J.-M. Malherbe, “Jules janssen, the birth of solar physics, the foundation of meudon observatory and the mont blanc adventure (1875-1895),” *HAL CNRS*, Aug. 2022.
- [3] S. A. Hamouda, F. F. Alfarjani, and F. Y. Elfituri, “Sunspots production and relation to other phenomena: A review,” *International Journal of Science and Research Methodology*, 06 2018.
- [4] F. Peter, *Solar Astrophysics*. Cambridge research and instrumentation, 1990.
- [5] T. A. Nieminen, “Solar line asymmetries: Modelling the effect of granulation on the solar spectrum,” *arXiv*, Aug. 2017. arXiv:1708.06408 [astro-ph].
- [6] M. Ellwarth, B. Ehmann, S. Schäfer, and A. Reiners, “Convective characteristics of fe i lines across the solar disc,” *Astronomy and Astrophysics*, vol. 680, p. A62, Dec. 2023.
- [7] D. F. Gray and B. Oostra, “The solar-flux third granulation signature,” *The Astrophysical Journal*, vol. 852, p. 42, Jan. 2018.
- [8] D. F. Gray, “The third signature of stellar granulation,” *The Astrophysical Journal*, vol. 697, p. 1032, May 2009.
- [9] D. Hamilton and J. B. Lester, “A technique for the study of stellar convection: The visible solar flux spectrum,” *Publications of the Astronomical Society of the Pacific*, vol. 111, p. 1132, Sept. 1999.

- [10] D. Dravins, L. Lindegren, and A. Nordlund, “Solar granulation - influence of convection on spectral line asymmetries and wavelength shifts,” *Astronomy and Astrophysics*, vol. 96, pp. 345–364, Mar. 1981.
- [11] D. F. Gray and T. Pugh, “The third signature of granulation in bright-giant and supergiant stars,” *The Astronomical Journal*, vol. 143, p. 92, Mar. 2012.
- [12] A. Reiners, N. Mrotzek, U. Lemke, J. Hinrichs, and K. Reinsch, “The iag solar flux atlas: Accurate wavelengths and absolute convective blueshift in standard solar spectra,” *Astronomy and Astrophysics*, vol. 587, p. A65, Mar. 2016.
- [13] H. H. Plaskett, “Solar granulation,” *Monthly Notices of the Royal Astronomical Society*, vol. 96, p. 402, Mar. 1936.
- [14] B. Carroll and D. Ostlie, *An Introduction to Modern Astrophysics*. Cambridge University Press, 2017.
- [15] G. Nave, S. Johansson, R. C. M. Learner, A. P. Thorne, and J. W. Brault, “A new multiplet table for fe i,” *The Astrophysical Journal Supplement Series*, vol. 94, p. 221, Sept. 1994.
- [16] C. Allende Prieto and R. J. Garcia Lopez, “Fe i line shifts in the optical spectrum of the sun,” *Astronomy and Astrophysics Supplement Series*, vol. 129, pp. 41–44, Apr. 1998.
- [17] J. P. Boyd, *Solving Transcendental Equations: The Chebyshev Polynomial Proxy and Other Numerical Rootfinders, Perturbation Series, and Oracles*. SIAM, Oct. 2014.
- [18] J. S. Aponte, *Medición de la velocidad convectiva en la fotosfera solar*. Bachelor’s thesis, Universidad de los Andes, 2017.
- [19] D. F. Gray, “Empirical decoding of the shapes of spectral-line bisectors,” *The Astrophysical Journal*, vol. 710, p. 1003, Jan. 2010.
- [20] D. F. Gray and K. I. T. Brown, “Precise spectroscopic radial velocity measurements using telluric lines,” *Publications of the Astronomical Society of the Pacific*, vol. 118, p. 399, Mar. 2006.

- [21] D. F. Gray, *The Observation and Analysis of Stellar Photospheres*. Cambridge University Press, 3 ed., 2005.
- [22] F. Stief, J. Löhner-Böttcher, W. Schmidt, T. Steinmetz, and R. Holzwarth, “Convective blueshifts in the solar atmosphere - ii. high-accuracy observations of the fe i 6173.3 Å line and deviations of full-disk dopplergrams,” *Astronomy and Astrophysics*, vol. 622, p. A34, Feb. 2019.
- [23] B. Ryden, *Introduction to cosmology*. Cambridge University Press, 2016.
- [24] A. Cacciani, R. Briguglio, F. Massa, and P. Rapex, “Precise measurement of the solar gravitational red shift,” *Celestial Mechanics and Dynamical Astronomy*, vol. 95, pp. 425–437, May 2006.